Finite-temperature optical conductivity with density-matrix renormalization group methods for the Holstein polaron and bipolaron with dispersive phonons

David Jansen [●],[1] Janez Bonča,[2,3] and Fabian Heidrich-Meisner [●][1]

[1]*Institut für Theoretische Physik, Georg-August-Universität Göttingen, D-37077 Göttingen, Germany*
[2]*J. Stefan Institute, 1000 Ljubljana, Slovenia*
[3]*Faculty of Mathematics and Physics, University of Ljubljana, 1000 Ljubljana, Slovenia*

A comprehensive picture of polaron and bipolaron physics is essential to understand the optical absorption spectrum in many materials with electron-phonon interactions. In particular, the finite-temperature properties are of interest since they play an important role in many experiments. Here, we combine the parallel two-site time-dependent variational principle algorithm (p2TDVP) with local basis optimization (LBO) and purification to calculate time-dependent current-current correlation functions. From this information, we extract the optical conductivity for the Holstein polaron and bipolaron with dispersive phonons at finite temperatures. For the polaron in the weak and intermediate electron-phonon coupling regimes, we analyze the influence of phonon dispersion relations on the spectra. For strong electron-phonon coupling, the known result of an asymmetric Gaussian is reproduced for a flat phonon band. For a finite phonon bandwidth, the center of the Gaussian is either shifted to larger or smaller frequencies, depending on the sign of the phonon hopping. We illustrate that this can be well understood by considering the Born-Oppenheimer surfaces. Similar behavior is seen for the bipolaron for strong coupling. For the bipolaron with weak and intermediate coupling strengths and a flat phonon band, we obtain two very different spectra. The latter also has a temperature-dependent resonance at a frequency below the phonon frequency.

I. INTRODUCTION

The interaction of an electron with lattice vibrations leads to the formation of a quasiparticle called a polaron, see, e.g., Ref. [1] for a review. Such a quasiparticle formation is of both theoretical and experimental interest since it is responsible for many material properties, e.g., in manganites [2–5], lead halide, and hybrid perovskites [6–9]. Since one way to experimentally study polaron physics is optical absorption spectroscopy, key insights into such materials can result from a better understanding of the optical excitation spectrum of these quasiparticles. These optical excitations allow for, e.g., the detection of small polarons, see, e.g., Refs. [10–12]. In several cases, theory and experiments were successfully combined to extract information about polarons in manganites, see, e.g., Refs. [10,12–14].

Experiments are inevitably conducted at finite temperatures. This calls for a comprehensive understanding of the temperature dependence of the polaron optical conductivity. For example, in Ref. [15], absorption spectra were used to investigate films of doped manganites by decreasing temperature, with a transition from a paramagnetic into a ferromagnetic phase. This led to the detection of a transition from small to large polarons. Furthermore, recent theoretical work has pointed out the importance of bipolaron formation for high-temperature superconductivity [16] and the experiments conducted in Ref. [17] emphasize the role of bipolarons in the pseudogap formation in the quasi-one-dimensional material $(TaSe_4)2I$.

An prototype microscopic model, capturing the interaction between electrons and optical phonons, is the Holstein model [18]. This model consists of electrons which can move around and interact with local harmonic oscillators. Despite its apparent simplicity, the Holstein model captures essential elements of both single polaron and bipolaron physics. Further, it also exhibits a transition from a charge-density wave (CDW) to a Tomanga-Luttinger liquid (TLL) at half filling in one dimension (see, e.g., Refs. [19,20] for phase diagrams). Due to their importance, the Holstein-polaron model [21–36], the Holstein model at finite filling [19,20,37–43], the Holstein-Hubbard model [44–54], and other similar systems [55–58] have been subject to intense and ongoing theoretical research.

Recent work has pointed out the effects of phonon hopping on CDW formation [59], thermalization properties of a polaron interacting with hard-core bosons [60], the polaron effective mass, the ground-state optical conductivity, and spectral functions [36,61,62]. In this work, we compute the real part of the optical conductivity for the Holstein polaron and bipolaron with dispersive optical phonons at different temperatures. We study weak, intermediate, and strong electron-phonon coupling strengths and work in the intermediate phonon frequency and electron-hopping regime. The combination of different interaction strengths together with a phonon dispersion for the polaron and bipolaron at finite temperatures extends and complements previous studies of the optical conductivity in the Holstein model, e.g., in Refs. [36,38,63–68].

The goal of this work is to characterize how the main features of small and large polarons in a Holstein-type system appear in the optical conductivity. By varying temperature and the phonon bandwidth, we extend the understanding of the basic mechanisms in such theoretical Hamiltonians, which incorporate essential physics induced by electron-phonon interaction. This constitutes an essential step in detecting such features, or lack thereof, in experimental data. Some of our key findings are that a finite phonon bandwidth shifts the center of the optical conductivity to higher or lower frequencies, depending on its shape. This holds for both the polaron and the bound bipolaron. Furthermore, the effect remains even when the temperature is increased enough to significantly alter the spectrum. For small electron-phonon coupling, the polaron-bipolaron spectrum remains similar up to a scaling factor. As the electron-phonon coupling is increased, key distinctions appear, such as a two-phonon emission maximum and a temperature-dependent resonance for the bipolaron, and a stable maximum at the one phonon emission peak for the polaron and only a weak temperature dependence on the spectrum (for the temperatures looked at here).

Computing finite-temperature transport properties of quantum systems can be a challenging task, see Ref. [69] for a review of one-dimensional systems. To compute the optical conductivity, we use a density-matrix renormalization group (DMRG) based method. DMRG [70–72] with matrix-product states (MPS) has already been extensively used to study one-dimensional systems, see, e.g., Refs. [73–81]. One drawback of DMRG is the unfavorable scaling for systems with a large local Hilbert space, as is the case for the Holstein model. For this reason, several schemes to treat these systems more efficiently have been suggested [82–85]. In Ref. [35], we successfully combined the finite-temperature method of purification [73] with tDMRG [74] and local basis optimization (LBO) [82] to compute several spectral functions of the Holstein-polaron model.

Here, we propose a scheme to combine LBO with the two-site time-dependent variational principle algorithm (TDVP) [86–88]. This method is used to conduct the imaginary-time evolution needed to obtain thermal states for weak, intermediate, and strong electron-phonon coupling in the nonadiabatic regime of the Holstein model (the phonon frequency ω_0 is close to the electron tunneling amplitude t_0, $t_0 \approx \omega_0$). We then use parallel two-site TDVP [88] with LBO (p2TDVP-LBO) to compute the real-time evolution of the current-current correlation function in the ground state for all parameters and at low temperatures in the weak and intermediate coupling regimes. For the temperature $T/\omega_0 = 1$ and a strong electron-phonon coupling, p2TDVP becomes computationally too demanding and therefore we use the single-site TDVP algorithm (without LBO) instead. We demonstrate that this combination of methods provides access to the real part of the optical conductivity $\sigma'(\omega)$. We further add phonon hopping with a hopping amplitude $t_{\rm ph}$. This gives rise to the finite phonon bandwidth shown in Fig. 1. We impose $0 \leqslant |t_{\rm ph}|/\omega_0 \ll 1$ to model optical phonons. We also compute the real part of the optical conductivity for the bipolaron for weak and intermediate coupling strengths and $t_{\rm ph} = 0$. Lastly, we analyze the effect of different phonon dispersion relation and a strong electron-phonon coupling on $\sigma'(\omega)$ for the bipolaron.
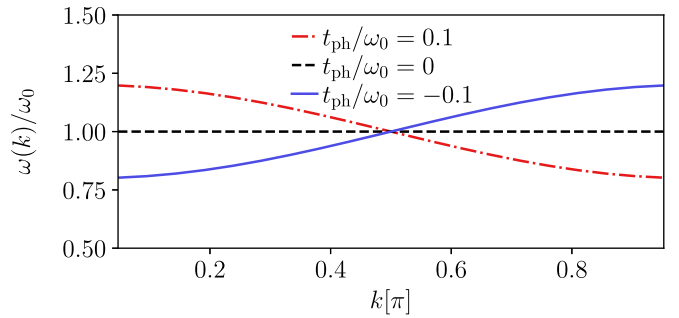

FIG. 1. Phonon dispersion relation $\omega(k)$ for optical phonons with phonon hopping, see Eq. (3). The hopping parameter is $t_{\rm ph}$ and the phonons have a finite bandwidth for $t_{\rm ph} \neq 0$.

We first test our algorithm by comparing the real part of the optical conductivity with that obtained for the ground state with the Lanczos method [89,90] in the weak and intermediate electron-phonon coupling regime. We find a very good agreement. Further, we derive a formula for the real part of the optical conductivity for the Holstein model with a finite phonon bandwidth based on the Born-Oppenheimer Hamiltonian and the Born-Huang ansatz [91,92]. This formula is consistent with our numerical data for a strong electron-phonon coupling for both the polaron and the bipolaron. In particular, we observe that in this regime, the optical spectrum is similar to that of an asymmetric Gaussian and a downwards phonon dispersion relation (a cosine with a maximum at small momenta, see Fig. 1) shifts the Gaussian to higher frequencies and an upwards phonon dispersion relation (a cosine with a maximum at large momenta, see Fig. 1) shifts it to lower frequencies. Additionally, the upwards phonon dispersion relation leads to less spectral weight at low frequencies for the temperatures studied in this work. These properties hold true for both the polaron and bipolaron.

In the weak and intermediate coupling regime and for the polaron, we see, as previously reported in Ref. [36], that an upwards dispersion relation leads to a continuous spectrum, and a downwards dispersion relation leads to a sequence of distinct peaks for the ground-state optical conductivity. For a weak electron-phonon coupling strength, the maximum of the spectrum shifts to lower frequencies as the temperature is increased and the different peaks merge. In the intermediate coupling regime, we also observe a significant increase of spectral weight for low frequencies, but the peaks remain well separated for the temperatures investigated here. For the bipolaron, we compare the weak and intermediate coupling for dispersionless phonons. We only detect very small changes in the spectrum for a weak electron-phonon coupling compared to twice the single-polaron curve. At intermediate coupling strengths, however, the spectrum differs significantly and an additional large resonance peak is resolved below ω_0.

This work is structured as follows. In Sec. II, we introduce the Holstein model with dispersive phonons and the optical conductivity, and in Sec. III, we derive a formula for the optical conductivity based on the Born-Oppenheimer Hamiltonian. Section IV introduces the p2TDVP-LBO algorithm. In Sec. V, we compare our Holstein-polaron ground-state results to those obtained with the Lanczos method and analytical

calculations. Section VI treats the polaron optical conductivity, and Sec. VII covers the bipolaron, both at finite temperature. Lastly, we conclude in Sec. VIII.

II. MODEL

A. The Holstein polaron and bipolaron

We consider the Holstein model [18] with one (polaron) and two (bipolaron) electrons. The Hamiltonian is defined as

$$\hat{H} = \hat{H}_{\text{kin}} + \hat{H}_{\text{ph}} + \hat{H}_{\text{e-ph}}. \quad (1)$$

The model has L sites and we use open boundary conditions. We set $\hbar = 1$ throughout this paper. The first term, the kinetic energy of the electrons, is

$$\hat{H}_{\text{kin}} = -t_0 \sum_{j=1,s=\uparrow,\downarrow}^{L-1} (\hat{c}_{j,s}^\dagger \hat{c}_{j+1,s} + \hat{c}_{j+1,s}^\dagger \hat{c}_{j,s}), \quad (2)$$

with $\hat{c}_{j,s}^\dagger$ ($\hat{c}_{j,s}$) being the electron creation (annihilation) operator on site j with spin s and the hopping amplitude t_0. The second term is the phonon energy, consisting of the harmonic oscillator energy and phonon kinetic energy:

$$\hat{H}_{\text{ph}} = \omega_0 \sum_{j=1}^{L} \hat{b}_j^\dagger \hat{b}_j + t_{\text{ph}} \sum_{j=1}^{L-1} (\hat{b}_j^\dagger \hat{b}_{j+1} + \hat{b}_{j+1}^\dagger \hat{b}_j), \quad (3)$$

where $\hat{b}_j^\dagger$ ($\hat{b}_j$) creates (annihilates) an optical phonon on site j with frequency ω_0. The phonons have a hopping amplitude t_{ph}. In this work, we always use $t_0/\omega_0 = 1$. The Hamiltonian in Eq. (3) can be diagonalized by going into quasimomentum basis by using the Fourier transformation for open boundary conditions

$$\hat{b}_k = \sqrt{\frac{2}{L+1}} \sum_{j=1}^{L} \sin(kj)\hat{b}_j, \quad (4)$$

where $k = \pi m_k/(L+1)$ and with $1 \leqslant m_k \leqslant L$. Then,

$$\hat{H}_{\text{ph}} = \sum_{k=\pi/(L+1)}^{\pi L/(L+1)} \omega(k)\hat{b}_k^\dagger \hat{b}_k, \quad (5)$$

with $\omega(k) = \omega_0 + 2t_{\text{ph}}\cos(k)$. $\omega(k)$ is the dispersion relation for the optical phonons with a finite bandwidth for $t_{\text{ph}} \neq 0$. In this work, we aim to model optical phonons with zero or small bandwidth and choose $|t_{\text{ph}}| \ll \omega_0$. For $t_{\text{ph}} < 0 (> 0)$, we refer to the phonons as having an upward (downward) dispersion relation. In Fig. 1, we illustrate the phonon dispersion relation for the values of t_{ph}/ω_0 used here.

The final term of the Hamiltonian in Eq. (1) is the electron-phonon coupling

$$\hat{H}_{\text{e-ph}} = \gamma \sum_{j=1}^{L} \hat{n}_j (\hat{b}_j^\dagger + \hat{b}_j), \quad (6)$$

with $\hat{n}_j = \hat{c}_{j,\uparrow}^\dagger \hat{c}_{j,\uparrow} + \hat{c}_{j,\downarrow}^\dagger \hat{c}_{j,\downarrow}$, and the coupling parameter γ. Note that since we do not include electron-electron repulsion in this work, we always deal with a bound bipolaron. Furthermore, we truncate the local phonon-Hilbert space to a finite maximum phonon number M. To characterize the

transition between a small and a large polaron, we introduce the dimensionless parameter

$$\lambda = N\frac{\gamma^2}{2t_0\omega_0}, \quad (7)$$

where $N = 1$ for the polaron and $N = 2$ for the bipolaron.

In order to obtain the real part of the optical conductivity, we first define the current-current correlation function as

$$C_T(t) = \langle \hat{J}(t)\hat{J}(0)\rangle_T, \quad (8)$$

where $\langle \ldots \rangle_T$ is the expectation value calculated in the canonical ensemble at temperature T. The current operator $\hat{J}$ is defined as

$$\hat{J} = it_0 \sum_{i=1,s=\uparrow,\downarrow}^{L-1} (\hat{c}_{j,s}^\dagger \hat{c}_{j+1,s} - \hat{c}_{j+1,s}^\dagger \hat{c}_{j,s}). \quad (9)$$

For calculations in the ground state $|GS\rangle$, we write $\lim_{T\to 0} C_T(t) = \lim_{T\to 0}\langle \hat{J}(t)\hat{J}(0)\rangle_T = \langle GS|\hat{J}(t)\hat{J}(0)|GS\rangle = C_{GS}(t)$. We further define its Fourier transformation as

$$C_T(\omega) = \int_{-\infty}^{\infty} e^{i\omega t} f(t)C_T(t)dt, \quad (10)$$

where $f(t)$ is a damping function ensuring a decay which we either choose to be $e^{-\eta|t|}$ or $e^{-\eta t^2}$, leading to a Lorenzian or Gaussian broadening in frequency space, respectively. In general, we obtain a higher accuracy of the moments of the correlation functions, see Appendix B, when using Gaussian broadening. Still, we will show data using Lorenzian broadening in Sec. V since this is used by the benchmark data. Furthermore, presenting results with different broadening functions demonstrates the small differences.

Our goal is to calculate the optical conductivity which can be split into real and imaginary part

$$\sigma(\omega) = \sigma'(\omega) + i\sigma''(\omega). \quad (11)$$

The imaginary part is related to the real part through the Kramers-Kronig relation [93]. The real part of $\sigma(\omega)$ can be extracted from the current-current correlation function via

$$\sigma'(\omega) = \frac{1 - e^{-\omega/T}}{2\omega}C_T(\omega). \quad (12)$$

For the ground state, we have

$$\sigma'_{T\to 0}(\omega) = \frac{1}{2\omega}C_{GS}(\omega). \quad (13)$$

III. OPTICAL CONDUCTIVITY BASED ON THE BORN-OPPENHEIMER HAMILTONIAN

An analytical formula for the optical conductivity for the Holstein polaron has been obtained in several different contexts and for different limiting cases, see, e.g., Refs. [66,94–96]. The theoretical results have been shown to fit both numerical, see, e.g., in Refs. [65,66], and experimental data, see, e.g., Refs. [10,12–14]. In this section, we obtain an expression for the real part of the optical conductivity based on the Born-Oppenheimer (BO) Hamiltonian and the Born-Huang formalism [91,92], which captures the influence of the finite phonon bandwidth for both the polaron and bipolaron. For more details, see Appendix C and Refs. [96–98].
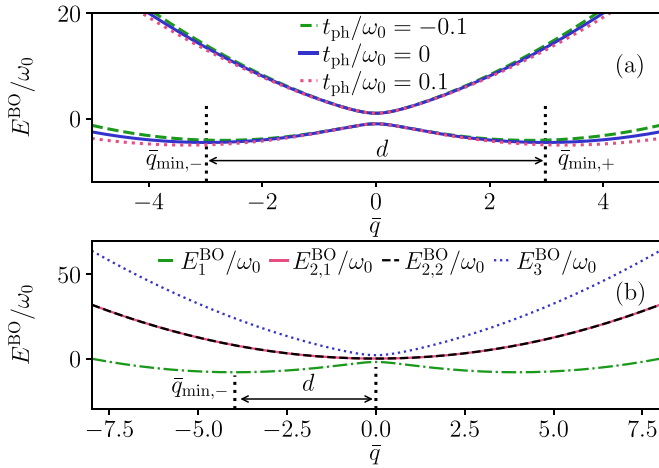
FIG. 2. Born-Oppenheimer surfaces for the polaron and bipo-laron in the Holstein dimer. (a) The two polaron Born-Oppenheimer surfaces with different phonon dispersion t_{ph}/ω_0. We use $\gamma/\omega_0 = 3$ and $t_0/\omega_0 = 1$. (b) The four Born-Oppenheimer surfaces for the Holstein-dimer bipolaron with $\gamma/\omega_0 = 2$, $t_{ph}/\omega_0 = 0$, and $t_0/\omega_0 = 1$.

We first rewrite Eq. (1) in terms of the phonon position and momentum operators, using that $\hat{b}_i = \sqrt{\frac{m\omega_0}{2}}(\hat{x}_i + \frac{i}{m\omega_0}\hat{p}_i)$ and $\hat{b}_i^\dagger = \sqrt{\frac{m\omega_0}{2}}(\hat{x}_i - \frac{i}{m\omega_0}\hat{p}_i)$. The total Hamiltonian has the form

$$\hat{H} = \hat{H}_{\text{kin}} + \sum_{i=1}^{L}\left(\gamma\sqrt{\frac{m\omega_0}{2}}\hat{n}_i(2\hat{x}_i)\right.$$
$$+ \frac{m\omega_0^2}{2}\left(\hat{x}_i^2 + \frac{1}{m^2\omega_0^2}\hat{p}_i^2 - \frac{1}{m\omega_0}\right)\right)$$
$$+ t_{\text{ph}}m\omega_0\sum_{i=1}^{L-1}\left(\hat{x}_i\hat{x}_{i+1} + \frac{1}{m^2\omega_0^2}\hat{p}_i\hat{p}_{i+1}\right). \quad (14)$$

We will now consider the Holstein dimer, i.e., $L = 2$, and go to the relative and center-of-mass coordinates with $\hat{q} = \frac{1}{\sqrt{2}}(\hat{x}_1 - \hat{x}_2)$ and $\hat{Q} = \frac{1}{\sqrt{2}}(\hat{x}_1 + \hat{x}_2)$. Using the fact that the center-of-mass coordinates $\hat{Q}$ are independent of the rest of the system for constant electron density, going in the adiabatic limit of slow phonons (sending all momenta to zero) and sending $\hat{q} \rightarrow q$, we can write the Born-Oppenheimer Hamiltonian as

$$\hat{H}_{\text{BO}} = \hat{H}_{\text{kin}} + \gamma[\bar{q}(n_1 - n_2)] + \frac{1}{2}\bar{q}^2(\omega_0 - t_{\text{ph}}). \quad (15)$$

Here, we have defined $\bar{q} = q\sqrt{\frac{1}{m\omega_0}}$. $\hat{H}_{\text{BO}}$ is now a 2×2 and a 4×4 matrix for the polaron and bipolaron, respectively, see, e.g., Refs. [99,100]. These Hamiltonians can be diagonalized and one obtains two or four Born-Oppenheimer surfaces, where two are degenerate in the latter case. We label the surfaces E_1^{BO} and E_2^{BO} for the polaron and E_1^{BO}, $E_{2,1}^{\text{BO}} = E_{2,2}^{\text{BO}}$, and E_3^{BO} for the bipolaron. The polaron and bipolaron surfaces are shown in Figs. 2(a) and 2(b) for some of the parameters used later in this work. The lowest surface has two minima which differ by a sign. We refer to these as $\bar{q}_{\text{min},\pm}$. The current operator from Eq. (9) can connect the states in the lowest and first excited surface while leaving the phonon configuration
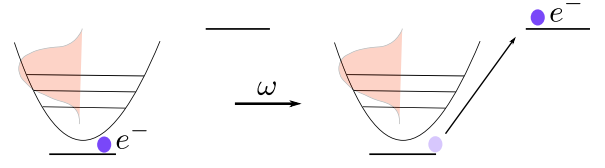

FIG. 3. Illustration of the Franck-Condon excitation, which is the process leading to Eq. (16). The electron is localized on one site in a potential due to the coupling to the phonons (illustrated by the shaded Gauss shape in the harmonic oscillator). Shining light with frequency $\omega = 2E_p$ will lead to the electron escaping the potential generated by the phonons and moving to the next site. During this process, the phonon configuration remains unchanged. This corresponds to a diagonal transition from the lower to the upper Born-Oppenheimer surface in Fig. 2(a).

invariant. This process, also known as a Franck-Condon ex-citation, is illustrated in Fig. 3 and corresponds to a vertical transition into the next surface at a fixed $\bar{q}$. When $|\bar{q}_{\text{min},\pm}|$ is large, this can be approximated as a transition between two harmonic oscillator potentials separated by a distance d and with an energy shift Δ_E. This leads to

$$\sigma_{SC}(\omega) = N\frac{1 - e^{-\omega/T}}{\omega}t_0^2\sqrt{\frac{4\pi}{d^2\coth\left(\frac{\tilde{\omega}_0}{2T}\right)\tilde{\omega}_0^2}}$$
$$\times e^{-\left(\Delta_E + \frac{d^2\tilde{\omega}_0}{2} - \omega\right)^2/\left(d^2\tilde{\omega}_0^2\coth\left(\frac{\tilde{\omega}_0}{2T}\right)\right)}. \quad (16)$$

Here, we set $\tilde{\omega}_0 = \omega_0 - t_{\text{ph}}$. For the Holstein polaron, $d = 2\bar{q}_{\text{min}}$ and $\Delta_E = 0$. For the Holstein bipolaron, we have $d = \bar{q}_{\text{min}}$ and $\Delta_E = E_1^{\text{BO}}(\bar{q}_{\text{min}})$, as illustrated in Fig. 2. Note that Eq. (16) is an asymmetric Gaussian around $\Delta_E + d^2\tilde{\omega}_0$ which is the energy difference between the lowest and the first ex-cited Born-Oppenheimer surface. For the polaron, everything can be solved analytically and one gets $\bar{q}_{\text{min},\pm} = \pm\frac{\sqrt{\gamma^4 - \tilde{\omega}_0^2 t_0^2}}{\tilde{\omega}_0\gamma}$. For the bipolaron, we obtain the Born-Oppenheimer surfaces numerically. In the case of the polaron, with $T \rightarrow 0$, $\gamma \gg t_0$ and $t_{\text{ph}} = 0$, we have $\bar{q}_{\text{min},\pm} = \pm\frac{\gamma}{\omega_0}$ and

$$\sigma_{SC}(\omega) = \frac{t_0^2}{\omega}\sqrt{\frac{\pi}{\frac{\gamma^2}{\omega_0}\omega_0}}e^{-\left(2\frac{\gamma^2}{\omega_0} - \omega\right)^2/\left(4\frac{\gamma^2}{\omega_0}\omega_0\right)}$$
$$= \frac{t_0^2}{\omega}\sqrt{\frac{\pi}{E_P\omega_0}}e^{-(2E_P - \omega)^2/(4E_P\omega_0)}, \quad (17)$$

which is the well-known result of an asymmetric Gaussian around twice the polaron binding energy $E_P = \gamma^2/\omega_0$.

IV. METHODS

There have already been many applications utilizing the matrix-product state formalism for finite temperature calcu-lations, see, e.g., Refs. [73,77–80,101,102]. In this work, we use purification [73,77,78,80,103]. In this scheme, one simu-lates the thermal density matrix of the system by introducing ancillary sites, thus doubling it. The density matrix at the desired temperature T can then be obtained by starting with the infinite-temperature state, imaginary time evolving it to the inverse temperature $1/(2T)$ and then tracing out the an-cillary sites. In other words, one obtains the thermal state
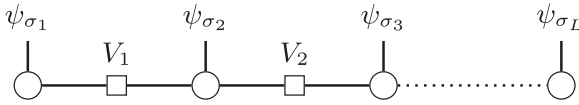
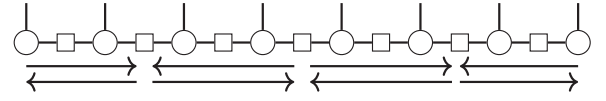FIG. 4. Matrix-product state in the inverse canonical form.

FIG. 5. Sweeping scheme of the pTDVP and pDMRG algorithms. One process starts sweeping either to the left or to the right as indicated by the arrows. At each contact point, the local tensors are shared and one process performs the sweeping step at the boundary. The resulting local tensor is then transported to its corresponding process and the sweeping is then continued in the opposite direction. In this example, the program would run on 4 processes.

living in the physical and ancillary Hilbert spaces, H_P and H_A, respectively, i.e., $|\psi_T\rangle \in H_P \otimes H_A$. The thermal expectation value of an observable $\hat{O}$ acting on a state in H_P is given by $\langle\hat{O}\rangle_T = \langle\psi_T|\hat{O}|\psi_T\rangle$. The state $|\psi_\infty\rangle$ can often be obtained either analytically or by finding the ground state of a suitable Hamiltonian [104], and $|\psi_T\rangle$ can be calculated by conducting imaginary time evolution on $|\psi_\infty\rangle$. Note that even though the infinite-temperature state is artificial for our implementation of the Holstein model due to the finite phonon truncation M, this method still captures the correct low-temperature physics, see Ref. [35]. There, a detailed description of how to obtain $|\psi_\infty\rangle$ for the Holstein polaron model is also given.

To obtain the time-dependent correlation functions from Eq. (8), one needs to carry out a real-time evolution after the imaginary-time evolution. The real-time evolution is, however, not carried out on $|\psi_T\rangle$, but rather on the state $|\phi_T\rangle$, which is obtained by acting on the thermal states $|\psi_T\rangle$ with the current operator $\hat{J}$, $|\phi_T\rangle = \hat{J}|\psi_T\rangle$. The real-time evolution of $|\phi_T\rangle$ is the computationally most costly part of our procedure.

There are several ways to time evolve matrix-product states, see Ref. [81] for a review, including the time-evolution block decimation (TEBD) algorithm, see Ref. [76], which also has a parallel implementation [105], and the time-dependent variational principle (TDVP) algorithm, see, e.g., Refs. [86,87,106–109]. In this work, we use the single-site TDVP, the two-site TDVP, and the parallel two-site TDVP (p2TDVP) algorithms introduced in Ref. [88]. We tailor the latter two specifically for electron-phonon systems with local basis optimization (LBO) [82]. Since the single-site and two-site TDVP are standard in the literature [81,86,87], we will, in Sec. IV A, only review the key ideas of parallelization of the two-site TDVP, and focus on how we incorporate LBO into the algorithm. We emphasize that the main idea of the parallelization of TDVP is based on the parallel ground-state DMRG (pDMRG) method introduced by Stoudenmire and White in Ref. [110] and that both the pDMRG and the pTDVP algorithms are described comprehensively in Refs. [110] and [88], respectively.

A. Parallel two-site time-dependent variational principle

For both pDMRG and p2TDVP, the first step is to bring the matrix-product state into the inverse canonical-gauge form

$$|\psi\rangle = \sum_{\vec{\sigma}} \psi_{\sigma_1} V_1 \psi_{\sigma_2} V_2 \ldots V_{L-1} \psi_{\sigma_L} |\vec{\sigma}\rangle. \quad (18)$$

Here, for a clearer notation, we will not write the bond indices unless they are specifically needed, and $|\vec{\sigma}\rangle = |\sigma_1, \sigma_2, \ldots, \sigma_L\rangle$, with σ_l being the physical state on site l. The state is depicted in Fig. 4. For the Holstein polaron model, $|\sigma_l\rangle$ consists of the local electron and phonon state $|\sigma_l\rangle = |n_e, n_{ph}\rangle$, with $n_e = \{0, 1\}$ and $n_{ph} = \{0, \ldots, M\}$.

Equation (18) can easily be obtained from the state in the canonical gauge [76,111]

$$|\psi\rangle = \sum_{\vec{\sigma}} \Gamma_{\sigma_1} \Lambda_1 \Gamma_{\sigma_2} \Lambda_2 \ldots \Lambda_{L-1} \Gamma_{\sigma_L} |\vec{\sigma}\rangle, \quad (19)$$

by inserting $V_j \Lambda_j = \mathbb{1}$ and defining $\psi_{\sigma_j} = \Lambda_{j-1} \Gamma_{\sigma_j} \Lambda_j$. The key ingredient of pDMRG is to partition the wave function from Eq. (18) onto several processes which each do their DMRG sweep and only communicate when the respective processes reach their corresponding boundaries. To make this as efficient as possible, one lets two processes start sweeping in different directions and communicate upon return. The scheme is sketched in Fig. 5.

The serial TDVP algorithm can be formulated similarly as DMRG, but by solving local time-dependent equations. For each update, here illustrated for the left-to-right sweep, one proceeds by first computing $\theta_{\alpha\beta} = \psi_{\sigma_i} V_i \psi_{\sigma_{i+1}}$, where the index α (β) contains the local degree of freedom σ_i (σ_{i+1}) and the left (right) bond m_l (m_r), i.e., $\alpha = (\sigma_i, m_l)$ and $\beta = (\sigma_{i+1}, m_r)$. The tensor $\theta_{\alpha\beta}$ is updated by solving the equation

$$\dot{\theta}_{\alpha\beta}(t) = \sum_{\alpha', \beta'} -i \frac{dt}{2} H^{\text{eff}}_{\alpha\beta\alpha'\beta'} \theta_{\alpha'\beta'}(t), \quad (20)$$

where $H^{\text{eff}}_{\alpha\beta\alpha'\beta'}$ is the effective two-site Hamiltonian, calculated by contracting the rest of the matrix-product state with the matrix-product operator Hamiltonian, see e.g., Refs. [72,81,88] for details. Equation (20) has the solution

$$\theta_{\alpha\beta}\left(t + \frac{dt}{2}\right) = \sum_{\alpha', \beta'} e^{-i\frac{dt}{2} H^{\text{eff}}_{\alpha\beta\alpha'\beta'}} \theta_{\alpha'\beta'}(t). \quad (21)$$

Consecutively, a singular value decomposition (SVD) is performed on the updated $\theta_{\alpha\beta} = A_{m_l\sigma_i} \Lambda_i B_{\sigma_{i+1}m_r}$ and $V_i \Lambda_i$ is inserted. We then write $\psi_{\sigma_i} = A_{m_l\sigma_i} \Lambda_i$ and $\psi_{\sigma_{i+1}} = \Lambda_i B_{\sigma_{i+1}m_r}$. For the discussion of the local basis optimization in the algorithm, we refer to solving Eq. (20) as step one and the following SVD as step two. Lastly, the effective one-site Hamiltonian $H^{\text{eff}}_{\gamma\gamma'}$ for site $j + 1$ is computed and ψ_γ is evolved backwards in time by solving

$$\psi_\gamma(t) = \sum_{\gamma'} e^{+i\frac{dt}{2} H^{\text{eff}}_{\gamma\gamma'}} \psi_{\gamma'}\left(t + \frac{dt}{2}\right), \quad (22)$$

where we wrote all indices of $\psi_{\sigma_{i+1}}$ as γ for brevity. The same process is then repeated for sites $i + 1$ and $i + 2$. Similar to pDMRG, one can partition the system for p2TDVP. We illustrate this in Fig. 5. This is done under the assumption that the inverse canonical form is approximately preserved

for small dt. Thereafter, one assigns each partition to an individual process together with the corresponding effective Hamiltonian. For the truncation in the SVDs, we discard all singular values such that

$$\sum_{\text{discarded } \eta} s_\eta^2 / \left(\sum_{\text{all } \eta} s_\eta^2 \right) < \epsilon_{\text{bond}}. \tag{23}$$

B. Local basis optimization

We now discuss how we incorporate the local basis optimization in the 2TDVP algorithm. This procedure is independent of whether the 2TDVP is run serially or in parallel. The idea of LBO [82] is to find a so-called optimal basis in which the state can be represented efficiently and truncated with a negligible error. LBO has already been used in many applications, see, e.g., Refs. [31,35,38,41,43,112,113]. To obtain the transformation matrices into an optimal basis, one first computes the reduced density matrix from, in our algorithm, the two-site tensor

$$\rho_{\sigma_i \sigma_i'} = (\theta \theta^\dagger)_{\sigma_i \sigma_i'}, \tag{24}$$

where all remaining indices have been contracted. $\rho_{\sigma_i \sigma_i'}$ is then diagonalized

$$\rho = R^\dagger W R. \tag{25}$$

The matrix R transforms the site from the physical basis σ_i to the optimal basis $\tilde{\sigma}_i$ and W is a diagonal matrix with the values w_α. The truncation of the optimal basis from the local dimension d into the dimension d_{LBO} is done based on the magnitude of the eigenvalues w_α, which, in many cases, decay exponentially, see, e.g., Refs. [30,43]. When diagonalizing the reduced density matrices in Eq. (24) to obtain the optimal basis, the smallest eigenvalues w_α are discarded such that the truncation error is below a threshold:

$$\sum_{\text{discarded } \eta} w_\eta / \left(\sum_{\text{all } \eta} w_\eta \right) < \epsilon_{\text{LBO}}. \tag{26}$$

There are two costly operations where a transformation of the physical index to an optimal basis can be beneficial. The most costly operation of the algorithm is the contraction of the effective Hamiltonian $H^{\text{eff}}_{\alpha\beta\alpha'\beta'}$ with the local tensor $\theta_{\alpha'\beta'}$ needed to solve Eq. (20) in step one. This has a cost of order $\mathcal{O}(d^3 m^2 D^2 + d^2 m D^3)$, where m is the bond dimension of the Hamiltonian and D the bond dimension of the state. We solve Eq. (20) with a fourth-order Runge-Kutta algorithm (RK4), see, e.g., Ref. [114] for an application of RK in the context of DMRG.

The RK4 algorithm consists of approximating $\theta_{\alpha\beta}(t + \frac{dt}{2})$ as

$$\theta_{\alpha\beta}\left(t + \frac{dt}{2}\right)$$
$$= \theta_{\alpha\beta}(t) + \frac{-idt}{2}\frac{1}{6}\left(k^1_{\alpha\beta} + 2k^2_{\alpha\beta} + 2k^3_{\alpha\beta} + k^4_{\alpha\beta}\right), \tag{27}$$

where for each k^j, we must contract the effective Hamiltonian with a two-site tensor. To incorporate LBO into the algorithm (RK4-LBO), we first obtain the transformation matrices into

the local optimal basis states $\tilde{\sigma}_i$ and $\tilde{\sigma}_{i+1}$ from $\theta_{\alpha\beta}$ as previously explained. We then transform the two sites of the effective Hamiltonian and $\theta_{\alpha\beta}$ into this new basis, $H^{\text{eff}}_{\alpha\beta\tilde{\alpha}\tilde{\beta}}$ and $\theta_{\tilde{\alpha}\tilde{\beta}}$, where $\tilde{\alpha} = (\tilde{\sigma}_i, m_l)$. Then, we compute

$$k^1_{\alpha\beta} = \sum_{\tilde{\alpha}'\tilde{\beta}'} H^{\text{eff}}_{\alpha\beta\tilde{\alpha}'\tilde{\beta}'} \theta_{\tilde{\alpha}'\tilde{\beta}'}(t). \tag{28}$$

We proceed by calculating

$$k^2_{\alpha\beta} = \sum_{\tilde{\alpha}'\tilde{\beta}'} H^{\text{eff}}_{\alpha\beta\tilde{\alpha}'\tilde{\beta}'} \left(\theta(t) + \frac{-idt}{2}\frac{1}{2}k^1 \right)_{\tilde{\alpha}'\tilde{\beta}'}, \tag{29}$$

but now $\tilde{\alpha}$ and $\tilde{\beta}$ are the optimal basis states extracted from the tensor $(\theta(t) + \frac{-idt}{2}\frac{1}{2}k^1)_{\alpha\beta}$. A similar procedure is used to obtain k^3 and k^4. One first adds the needed tensors and then obtains the new optimal basis states before contracting with the environment. Note that it is not ensured that one gains a computational benefit from the algorithm. As mentioned earlier, one must first create the reduced density matrices at a cost of order $\mathcal{O}(D^2 d^3)$, diagonalize them at a cost of order $\mathcal{O}(d^3)$, apply the transformation matrices at a cost of order $\mathcal{O}(D^2 d^2 d_{\text{LBO}})$, and add the tensors at a cost of order $\mathcal{O}(D^2 d^2)$ to get a cost for the contraction of order $\mathcal{O}(d^2 d_{\text{LBO}} m^2 D^2 + d^2 m D^3)$. In practice, however, we find this scheme to lead to a computational speed-up in many situations, compared to only implementing step two. This is also due to the additional benefit of the optimal basis on the many subleading tensor contractions.

A common approach to solve Eq. (20) is to use a Krylov method. While the RK4 algorithm is nonunitary, we also compare some of our data to that obtained using a Krylov solver without LBO and the tDMRG-LBO time-evolution algorithm used in Ref. [35]. The error appears to be negligible in the cases studied here. A comparison and discussion of the different algorithms are contained in Appendix A. Alternatively, one could also apply the local basis transformation when using a Krylov solver, thus needing to find the optimal basis for each Krylov vector. In our tests, this seems to require more optimal basis states than the RK4 scheme. This is addressed in Appendix A as well.

To implement the LBO before the SVD in step two, all one needs to do is to get the local basis of $\theta_{\alpha\beta}(t + \frac{dt}{2})$, then transform the tensor into $\theta_{\tilde{\alpha}\tilde{\beta}}(t + \frac{dt}{2})$, and carry out the singular value decomposition before transforming the tensor back to the bare basis. This step has the cost $\mathcal{O}(d^3 + D^2 d^3)$, but the cost of the SVD becomes of the order $\mathcal{O}(D^3 d^3_{\text{LBO}})$.

In our experience, only implementing step two alone is sufficient to gain a significant computational speed up. This can easily be incorporated into ground-state DMRG algorithms as well. A discussion of the number of local states needed is presented in Appendix A.

For the imaginary-time evolution used to obtain all the thermal states in this work, we only implement step two and use a Krylov solver for the local differential equations in Eq. (20). Our reason is that the imaginary-time evolution is less costly, and RK4 is unstable in our calculations for all but very small imaginary time steps $d\tau$. This computation is also run serially. To ensure that the low bond dimension of the initial states does not lead to a significant projection

error, we compared the states to those obtained using tDMRG for the polaron. For both the polaron and bipolaron, we also compared the states where we imaginary-time evolved using a higher bond dimension through the sub-space expansion introduced in Ref. [108]. If $|\psi_A\rangle$ and $|\psi_B\rangle$ are states obtained with different imaginary time-evolution schemes, we had $|1 - \langle\psi_A|\psi_B\rangle|$ of the order of $\mathcal{O}(10^{-6})$ in all cases.

For the real-time evolution, we implement both steps one and two and refer to the algorithm as p2TDVP-LBO. Note that when carrying out the real-time evolution, we simultaneously time-evolve the part of the state in the ancillary space back in time to get a slower increase in the bond dimension [115–119]. While not an optimal procedure, see Ref. [120], this can easily be incorporated into the algorithm. We carry out the real-time evolution until $t_{\max}\omega_0$ and add $4\,t_{\max}\omega_0$ zeros to the signal for better resolution (zero padding) before the Fourier transformation. Alternatively, one can use linear prediction, see, e.g., Refs. [78,121,122], for a higher frequency resolution. We confirmed that both methods give consistent results for our data. Recently, another method for reaching longer times has been proposed [123].

For the real-time evolution, we use a time step $dt/\omega_0 = 0.01$ and for the imaginary-time evolution $d\tau/\omega_0 = 0.1$. When real-time evolving at high temperatures (here $T/\omega_0 = 1$) and in the large-coupling regime, we take advantage of the fact that the thermal states have a relatively large bond dimension (which increases further when we act with $\hat{J}$ on the state) and use a serial single-site TDVP algorithm. This is done since the bond dimension becomes unfeasible for our computational resources otherwise. Furthermore, this approach does not require the implementation of LBO for our applications, since the algorithm scales better with the local Hilbert space dimension. In this case, $\epsilon_{\mathrm{bond},J}$ indicates the cutoff at which we truncate after applying the current operator to the thermal state. Here, convergence is monitored by changing $\epsilon_{\mathrm{bond},J}$, even though the time-evolution scheme itself has a constant bond dimension. To make sure that small bond dimensions on some bonds do not lead to errors, we also compared the results to those obtained with a larger bond dimension by enforcing a minimum bond dimension when applying $\hat{J}$.

To further verify our results, we carefully compare the moments of the time-dependent correlation functions to their finite-temperature expectation values, see Appendix B for details. To test our algorithm, we also compare our ground-state optical conductivity to data obtained with the Lanczos method for weak and intermediate electron-phonon coupling. Furthermore, we check that our finite-temperature polaron data in the weak and intermediate electron-phonon coupling regime is consistent with those obtained with a different time-evolution method whenever possible, namely the tDMRG-LBO method used in Ref. [35]. Additionally, we monitor the f-sum rule in the large electron-phonon coupling regime. This is also contained in Appendix B. All calculations are done with the ITENSOR software library [124].

We now demonstrate how we control the convergence of the p2TDVP-LBO time evolution with respect to ϵ_{bond} and ϵ_{LBO}. This is illustrated in Fig. 6 for the real-time current-current correlation function for $\gamma/\omega_0 = \sqrt{2}$ and $t_{\mathrm{ph}}/\omega_0 = -0.1$. Figure 6(a) shows $\mathrm{Re}[C_T(t)]$ for a fixed ϵ_{LBO} and different ϵ_{bond}. The data illustrate that when ϵ_{bond} is chosen
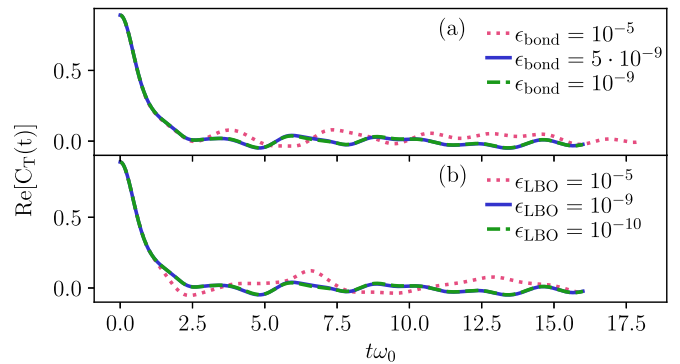

FIG. 6. (a) Real part of the current-current correlation function from Eq. (8) for $L = 20$, $M = 20$, $\gamma/\omega_0 = \sqrt{2}$, and $t_{\mathrm{ph}}/\omega_0 = -0.1$, computed in the ground state ($T/\omega_0 = 0$). We use a fixed $\epsilon_{\mathrm{LBO}} = 10^{-9}$ and different ϵ_{bond}. (b) Same as in (a) but with a fixed $\epsilon_{\mathrm{bond}} = 10^{-9}$ and different ϵ_{LBO}. The calculation is done with p2TDVP-LBO and is distributed onto four processes.

sufficiently small, the correlation functions become independent thereof and the curves are converged for our purposes. In Fig. 6(b), we show a similar plot but for a fixed ϵ_{bond}. As can be seen, both ϵ_{bond} and ϵ_{LBO} must be chosen carefully. We note that during this work, we have observed that, in some cases, one can obtain similar optical conductivities with the same key features even when the correlations functions still depend noticeably on cutoffs. One could control convergence by only monitoring the quality of the optical conductivity. We work with the stricter criteria of monitoring both the correlation functions and the optical conductivity as elaborated on above. Note that in some cases, small deviations could not be avoided with our computational resources.

V. GROUND-STATE RESULTS

In this section, we present the results for the real part of the optical conductivity obtained with p2TDVP-LBO for the ground state of the Holstein polaron. The ground state itself is obtained with ground-state DMRG. Our results are compared to calculations with the Lanczos method for weak and intermediate electron-phonon coupling. For strong coupling, we compare to Eq. (16).

A. Ground-state results in the weak- and intermediate-coupling regimes

We first look at the optical conductivity in the ground state for different electron-phonon coupling strengths and different phonon dispersion relations. The effects of the dispersion on the optical conductivity were thoroughly investigated in Ref. [36], however, we also describe the behavior here for self-consistency and to guide the discussion of the results at finite temperature.

We verify the correctness of our results by comparing them to the optical conductivity obtained with the Lanczos method. This method uses a constructed variational Hilbert space and allows for 28 phonons at the initial site of the electron, but fewer and fewer at the sites further away, see Ref. [36] for details. The Lanczos method has the advantage
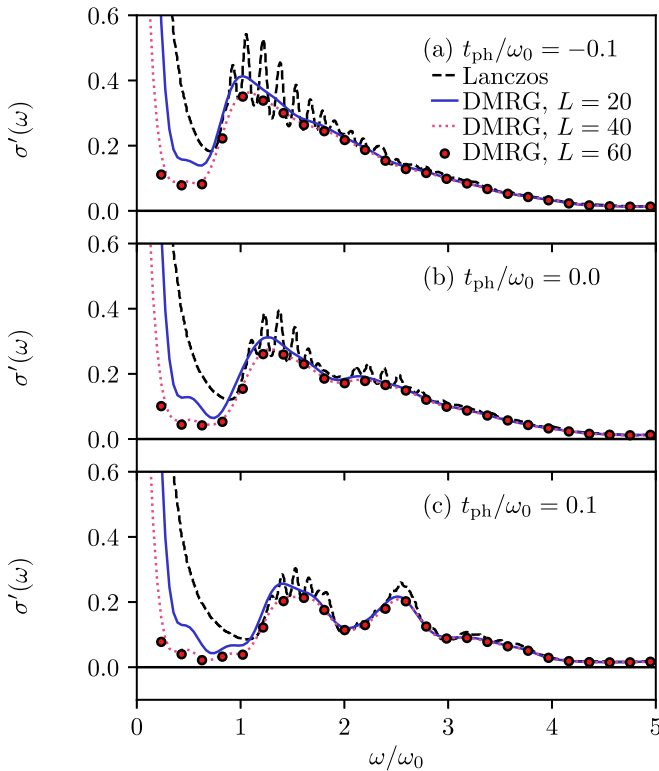
FIG. 7. (a) Real part of the optical conductivity for the Holstein polaron in the ground state for $\lambda = 1/2$, $M = 20$, $\epsilon_{\mathrm{Bond}} = \epsilon_{\mathrm{LBO}} = 10^{-9}$, and with $t_{\mathrm{ph}}/\omega_0 = -0.1$. (b) Same as in (a) but with and $t_{\mathrm{ph}}/\omega_0 = 0.0$. (c) Same as in (a) but with $t_{\mathrm{ph}}/\omega_0 = 0.1$. We show $L = 60, 40, 20$, and the time evolution is done up to $t_{\mathrm{max}}\omega_0 = 16$. We further use a Lorenzian broadening with $\eta = 0.1$. The black dashed line is the reference data computed with the Lanczos method. The DMRG simulations, obtained with p2TDVP-LBO, are distributed onto 12, 8, and 4 processes for $L = 60, 40$, and 20, respectively.

of computing the optical conductivity directly in frequency space and can easily extract the Drude weight. However, it has more difficulties in including many phonons and larger systems than the DMRG method. Lastly, the DMRG has an (in principle) straightforward extension to finite densities. In a setup where the Lanczos method cannot utilize the variational Hilbert space approach, the treatable system sizes will also be limited.

In Fig. 7, we show the real part of the optical conductivity in the Holstein-polaron model in the weak-coupling regime, $\lambda = 1/2$, for different values of the phonon hopping amplitude t_{ph}, calculated with the Lanczos method and p2TDVP-LBO for $L = 20, 40$, and 60. The first important result is that the p2TDVP-LBO method reproduces the incoherent part of $\sigma'(\omega)$ from the Lanczos method very accurately. Additionally, we see that we can access system sizes large enough to obtain results approximately independent thereof.

Figure 7(b) shows the real part of the optical conductivity at finite ω and a flat phonon band. The incoherent part is dominated by two peaks starting at approximately $\omega/\omega_0 = 1$ and 2. The appearance of a peak at $\omega/\omega_0 = 1$ is consistent with weak-coupling perturbation theory, see, e.g., Ref. [66], and stems from the one-phonon emission process. The width

of the peaks is also given by the possible changes in electron quasimomenta k_{el}. This is because the emitted phonon can have any quasimomentum due to the flat dispersion relation and the transition energies are thus dominated by the change in electron energy. Here, the biggest difference between the Lanczos and the p2TDVP-LBO data are visible. The Lanczos data exhibit a peak structure occurring due to the possible electron quasimomenta k_{el}, which we cannot resolve with p2TDVP-LBO due to the finite resolution coming from the limited times available and the large number of k_{el}.

When a small upward dispersion relation, $t_{\mathrm{ph}}/\omega_0 = -0.1$, is introduced, see Fig. 7(a), the distinction between the different phonon emission peaks disappears and the weight of the incoherent spectra gets slightly shifted to lower frequencies. The latter can be explained by the fact that the emitted phonon has an additional energy contribution of $\sim 2t_{\mathrm{ph}}$ due to the finite phonon bandwidth. As a result, the peak shifts to $\sim \omega_0 + 2t_{\mathrm{ph}}$. The transfer to higher quasimomentum states still remains rather unaffected since $|t_0/t_{\mathrm{ph}}| \gg 1$. Similar behavior of the second phonon peak leads to the monotonic decay of the incoherent spectra after the first maximum.

For $t_{\mathrm{ph}}/\omega_0 = 0.1$ in Fig. 7(c), we see the opposite effect. The one- and two-phonon emission peaks become more easily separable and their maxima get shifted to larger frequencies. This is consistent with the fact that every transition energy introduces the term $2t_{\mathrm{ph}}\cos(k)$. For small k, the energy differences correspond to larger frequencies whereas the opposite happens for larger k with $2t_{\mathrm{ph}}\cos(k) > 0$. In total, this leads to a shift of the peaks to higher frequencies and a suppression of their width.

We now turn to the intermediate coupling regime with $\lambda = 1$. The ground-state results are presented in Fig. 8. We show $t_{\mathrm{ph}}/\omega_0 = -0.1$ in Fig. 8(a), $t_{\mathrm{ph}}/\omega_0 = 0$ in Fig. 8(b), and $t_{\mathrm{ph}}/\omega_0 = 0.1$ in Fig. 8(c). Again, essentially the same incoherent structure is produced by both the Lanczos and p2TDVP-LBO method with small differences in some peak heights. In this regime, a small but finite phonon bandwidth has a significant impact on the optical conductivity. In general, the spectra broaden, signaling that the two and three phonon-emission processes play a more important role when the coupling is increased. Note that due to the small values for the dispersion, we do not observe the multi-phonon structure at $\omega < \omega_0$ for $t_{\mathrm{ph}} > 0$, as reported in Ref. [36]. Still, the same physical effects as in the weak-coupling case can be observed, although significantly enhanced. For example, the one- and two-phonon peak for $t_{\mathrm{ph}}/\omega_0 = 0.1$ in Fig. 8(c) are almost completely distinguishable. In conclusion, we see that the p2TDVP-LBO method can reproduce all the features from the Lanczos method very well in the incoherent part of the spectrum for both $\lambda = 1$ and $\lambda = 1/2$. Note that we observe some oscillations for low frequencies which we attribute to artifacts of the Fourier transformation. This was verified by comparing the DMRG data to only the regular part of the Lanczos data.

B. Ground state in the strong-coupling regime

We now turn to the ground-state optical conductivity in the strong-coupling regime with $\gamma/\omega_0 = 3$. As can be seen from Eq. (16) and by analyzing the Born-Oppenheimer surfaces
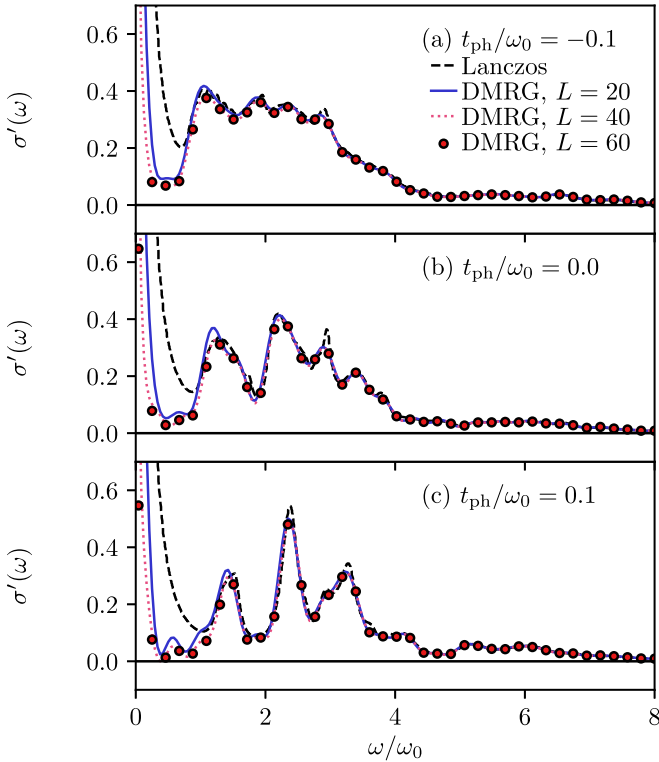
FIG. 8. (a) Real part of the optical conductivity for the Holstein polaron in the ground state for $\lambda = 1, M = 20, \epsilon_{\mathrm{Bond}} = \epsilon_{\mathrm{LBO}} = 10^{-9}$, and with $t_{\mathrm{ph}}/\omega_0 = -0.1$. (b) Same as in (a) but with and $t_{\mathrm{ph}}/\omega_0 = 0.0$. (c) Same as in (a) but with $t_{\mathrm{ph}}/\omega_0 = 0.1$. We show $L = 60$, 40, 20, and the time evolution is done up to $t_{\mathrm{max}}\omega_0 = 15$. We further use a Lorenzian broadening with $\eta = 0.08$. The black dashed line is the reference data computed with the Lanczos method. The DMRG simulations, calculated using p2TDVP-LBO, are distributed onto 12, 8 and 4 processes for $L = 60$, 40, and 20, respectively.

FIG. 9. (a) Real part of the optical conductivity for the Holstein polaron in the ground state for $\lambda = 4.5$. We further set $M = 35$, $\epsilon_{\mathrm{Bond}} = \epsilon_{\mathrm{LBO}} = 10^{-7}$, $L = 20$, and $t_{\mathrm{ph}}/\omega_0 = -0.1$. (b) Same as in (a) but with $t_{\mathrm{ph}}/\omega_0 = 0$. (c) Same as in (a) but with $t_{\mathrm{ph}}/\omega_0 = 0.1$. The blue solid line is the DMRG data and the dashed solid line is the analytical formula from Eq. (16). The vertical gray dashed lines show the respective energy differences between the Born-Oppenheimer surfaces at $\bar{q}_{\mathrm{min},-}$. The time-evolution is done up to $t_{\mathrm{max}}\omega_0 = 11$ and we use a Lorenzian broadening with $\eta = 0.1$. The simulation is distributed onto four processes for the DMRG calculations using p2TDVP-LBO.

in Fig. 2, the expectation is a shifted Gaussian around twice the polaron binding energy E_P for a flat phonon dispersion relation. With a finite phonon bandwidth, one expects the Gaussian to be shifted to either larger or smaller frequencies depending on the sign of t_{ph}. This central peak can be understood in terms of the Franck-Condon transition in the extreme adiabatic limit. There, the motion of the electron is so fast compared to that of the phonons that the electron is excited without changing the phonon configuration with an energy difference of $2E_P$. This process is sketched in Fig. 3. In Fig. 9, the results of the p2TDVP-LBO ground-state calculation for different phonon dispersion is plotted. We show the expression from Eq. (16) and the p2TDVP-LBO data for $t_{\mathrm{ph}}/\omega_0 = -0.1$ in Fig. 9(a), $t_{\mathrm{ph}}/\omega_0 = 0$ in Fig. 9(b), and $t_{\mathrm{ph}}/\omega_0 = 0.1$ in Fig. 9(c). Our numerical results are very well approximated by the analytic formula. Comparing Figs. 9(a)–9(c), it becomes clear that even a small but finite phonon bandwidth significantly alters the position of the maximum of the spectrum. A downwards phonon dispersion relation shifts the absorption spectrum to higher frequencies and an upwards phonon dispersion relation shifts it to lower frequencies. This is expected from inspecting the Born-Oppenheimer surfaces in Sec III. The vertical gray dashed lines in Fig. 9 indicate
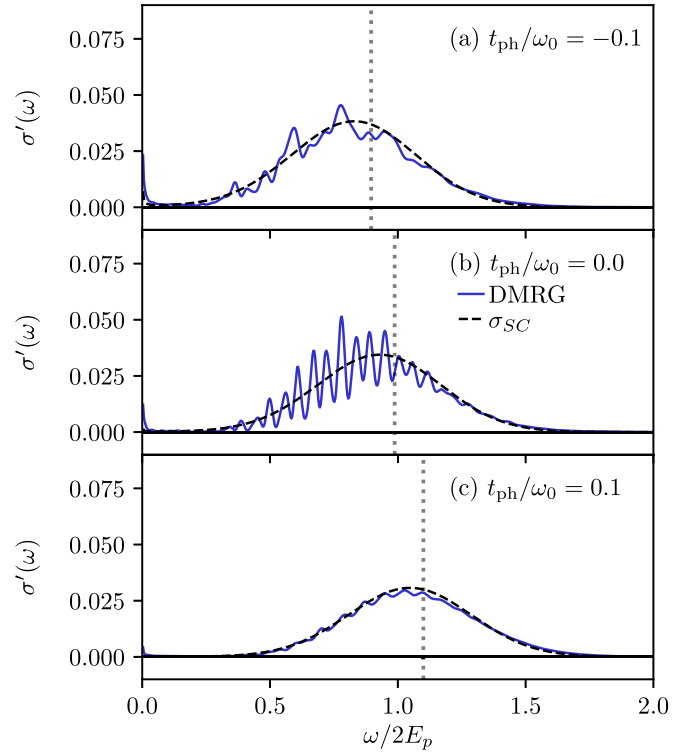
the energy differences between the two Born-Oppenheimer surfaces at the minimum of the lowest surface.

We conclude that our method also works well for a large electron-phonon coupling in the ground state, but we note that many local modes are needed in the local basis optimization. For example, the calculations in Figs. 7–9, required roughly 10, 15, and 30 local optimal basis states in both steps one and two of the algorithm. We also emphasize that, despite being calculated far from the adiabatic limit ($t_0/\omega_0 = 1$), our results agree well with the analytic predictions. Note that in Fig. 9, there is still a resilient M dependence in the amplitude of some peaks, most notably so in Fig. 9(b). This is further discussed in Appendix B.

VI. FINITE-TEMPERATURE RESULTS

A. Finite-temperature results in the weak and intermediate coupling regimes

We proceed by investigating how the real part of the optical conductivity changes when going from zero to finite temperatures. Figure 10 shows $\sigma'(\omega)$ for the Holstein polaron for $\lambda = 1/2$ at different temperatures and with different values of the phonon hopping amplitude t_{ph}. One can observe a similar
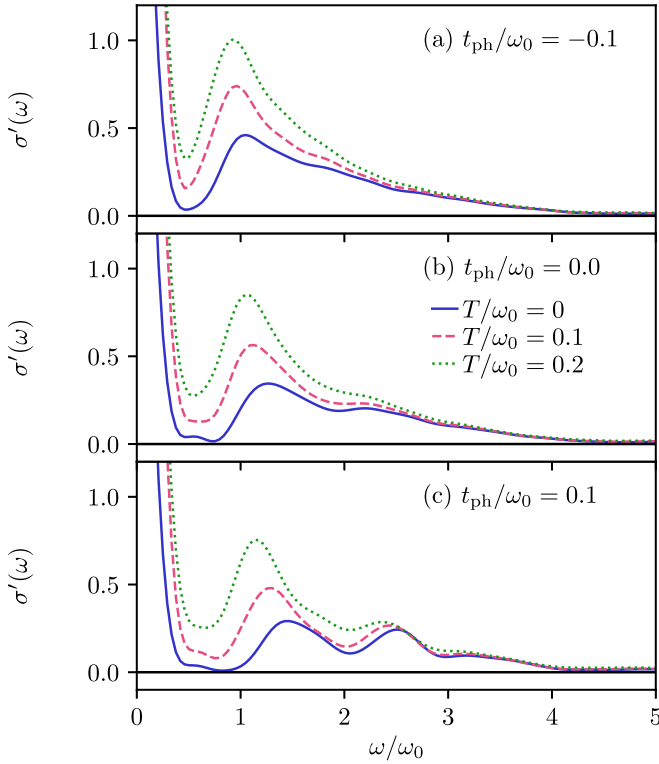
FIG. 10. (a) Real part of the optical conductivity at finite temperatures for $\lambda = 1/2$ and with $t_{ph}/\omega_0 = -0.1$. (b) Same as in (a) but with $t_{ph}/\omega_0 = 0$. (c) Same as in (a) but with $t_{ph}/\omega_0 = 0.1$. We further set $M = 20$, $L = 20$, and $\epsilon_{Bond} = \epsilon_{LBO} = 10^{-9}$. The time evolution is done up to $t_{max}\omega_0 = 15$ and we use a Gaussian broadening with $\eta = 0.1/(4\pi)$. The simulations are carried out with p2TDVP-LBO and distributed onto four processes for the ground-state calculations and onto eight processes at finite temperature.
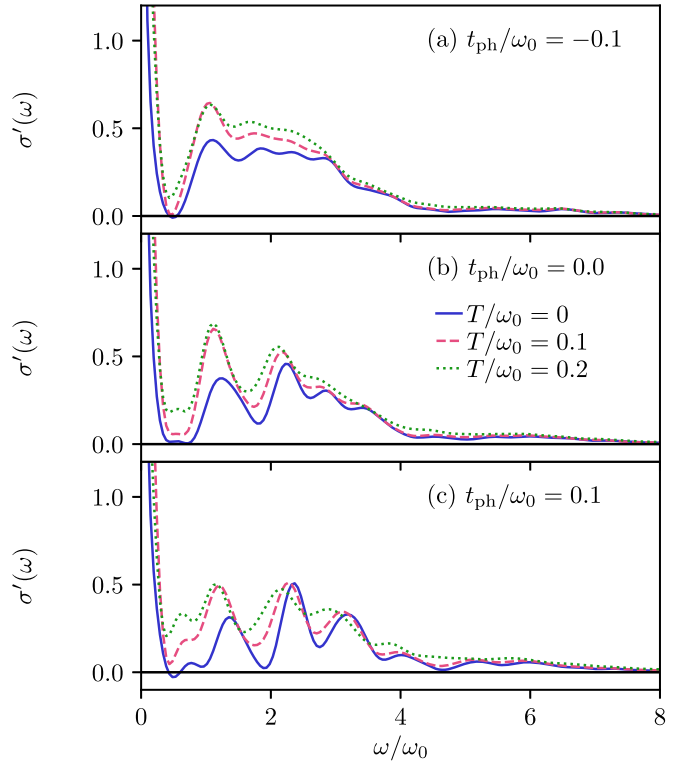

FIG. 11. (a) Real part of the optical conductivity at finite temperatures for $\lambda = 1$ and with $t_{ph}/\omega_0 = -0.1$. (b) Same as in (a) but with $t_{ph}/\omega_0 = 0$. (c) Same as in (a) but with $t_{ph}/\omega_0 = 0.1$. We further set $M = 20$, $L = 20$, and $\epsilon_{Bond} = \epsilon_{LBO} = 10^{-9}$ for $T/\omega_0 = 0$ and $\epsilon_{Bond} = 5 \times 10^{-9}$, $\epsilon_{LBO} = 10^{-9}$ for $T/\omega_0 = 0.1$, 0.2. The time evolution is done up to $t_{max}\omega_0 = 13$ and we use a Gaussian broadening with $\eta = 0.1/(4\pi)$. The simulations are carried out with p2TDVP-LBO and distributed onto four processes for the ground-state calculations and onto eight processes at finite temperature.

influence of the finite temperature for the upwards dispersion relation [$t_{ph}/\omega_0 = -0.1$ in Fig. 10(a)], a flat dispersion relation [$t_{ph}/\omega_0 = 0$ in Fig. 10(b)], and downwards dispersion relation [$t_{ph}/\omega_0 = 0.1$ in Fig. 10(c)]. Namely, there is a clear increase in spectral weight at low frequencies. This is consistent with other calculations in the weak-coupling regime [66] (although there in the adiabatic regime). This is due to the contribution of states previously thermally suppressed with a smaller energy difference than ω_0. We further see an increase in the one-phonon emission-peak amplitude. This is due to the enhanced population of higher quasimomentum states at a higher temperature, which now all contribute through one-phonon emission processes. The maximum one-phonon peak also shifts to lower frequencies, and the effect seems more apparent for $t_{ph}/\omega_0 = 0.1$ than for $t_{ph}/\omega_0 = -0.1$. We attribute this to the fact that the sign of the curvature in the polaron and phonon bands differ in the first case and is the same in the latter.

In the intermediate regime, $\lambda = 1$ in Fig. 11, there is a different influence of the finite temperature on the spectrum. Whereas higher T/ω_0 almost washes out the separate peak structure for $t_{ph}/\omega_0 = 0$, 0.1, and $\lambda = 1/2$, the peaks remain fairly well separated for all temperatures studied here when $\lambda = 1$. This is valid for $t_{ph}/\omega_0 = 0$ and $t_{ph}/\omega_0 = 0.1$ in Figs. 11(b) and 11(c), respectively. Furthermore, when

$t_{ph}/\omega_0 = -0.1$, the spectrum remains largely unaffected by temperature other than enhanced weight at lower frequencies. By decreasing η, we can observe small temperature dependent resonances at low frequencies for $\lambda = 1/2$, 1, and $t_{ph}/\omega_0 = 0$, 0.1 [this can still be seen in Fig. 11(c)], but from our available data, we cannot conclusively determine if they are physical or an artifact of the Fourier transformation. In this case, a higher frequency resolution would be necessary.

B. Finite-temperature results in the strong-coupling regime

We now analyze how the optical conductivity changes with temperature in the strong-coupling regime, i.e., $\lambda = 4.5$. The results can be seen in Figs. 12(a)–12(c) for the phonon dispersion $t_{ph}/\omega_0 = -0.1$, 0, and 0.1, respectively. The analytic formula for the optical conductivity, see Eq. (16), remains a good approximation in all cases in Fig. 12, even as the temperature is increased to $T/\omega_0 = 1$. Still, our data have less spectral weight at low frequencies. The reason is not obvious, but some deviations are to be expected since we are far away from the adiabatic limit. Further, we observe that the phonon dispersion relation affects the finite-temperature behavior. The upwards dispersion relation, see Fig. 12(a), leads to a larger contribution at low frequencies than the downward
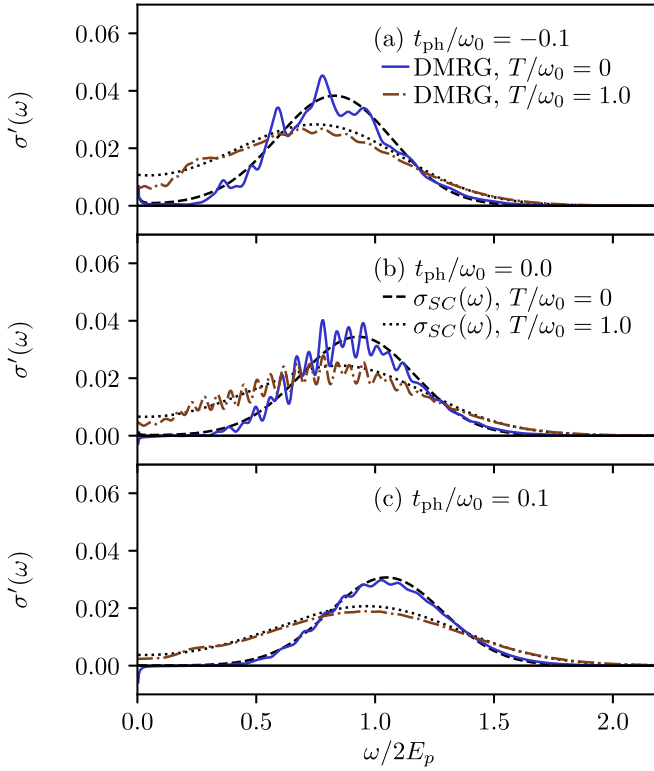
FIG. 12. (a) Real part of the optical conductivity at different temperatures for $\lambda = 4.5$ and with $t_{\mathrm{ph}}/\omega_0 = -0.1$. (b) Same as in (a) but with $t_{\mathrm{ph}}/\omega_0 = 0$. (c) Same as in (a) but with $t_{\mathrm{ph}}/\omega_0 = 0.1$. We further set $M = 35$, $L = 20$, and $\epsilon_{\mathrm{Bond}} = \epsilon_{\mathrm{LBO}} = 10^{-7}$ for the ground-state calculations. For the real-time evolution for $T/\omega_0 = 1.0$, we use single-site TDVP with $\epsilon_{\mathrm{bond},J} = 10^{-8}$ for $t_{\mathrm{ph}}/\omega_0 = -0.1$, 0.1 and $\epsilon_{\mathrm{bond},J} = 10^{-9}$ for $t_{\mathrm{ph}}/\omega_0 = 0$ (see Sec. IV for details). The time evolution is done up to $t_{\mathrm{max}}\omega_0 = 11$ and we use a Gaussian broadening with $\eta = 0.5/(4\pi)$. The black dashed and dotted lines are the analytical formula from Eq. (16). The ground-state DMRG results are distributed onto 4 processes and are calculated with p2TDVP-LBO.

dispersion relation in Fig. 12(c). Looking at the $\omega \rightarrow 0$ values, it appears that the thermally activated hopping plays a lesser role when there is a downwards than an upwards phonon dispersion relation. This is consistent with the depth of the lower Born-Oppenheimer surfaces increasing, as can be seen in Fig. 2. Furthermore, since the low quasimomenta phonons have higher energy for the downwards dispersion relation, the nondiagonal transition with a small change in electron quasimomenta is suppressed compared to the upwards dispersion relation case. Note that the resonance at $\omega = 2t_0$ seen in Ref. [65] for a small ω_0/t_0 can be qualitatively reproduced by our method (not shown here). We further mention that small finite-size effects can be seen in some of the oscillation amplitudes in the data shown in Fig. 12. This is illustrated in Appendix B.

VII. BIPOLARON RESULTS

We now proceed to study the real part of the optical conductivity of the Holstein bipolaron at finite temperature. In Fig. 13, we plot $\sigma'(\omega)$ for weak and intermediate electron-phonon coupling, $\lambda = 1/2$, 1, with $t_{\mathrm{ph}}/\omega_0 = 0$. We observe
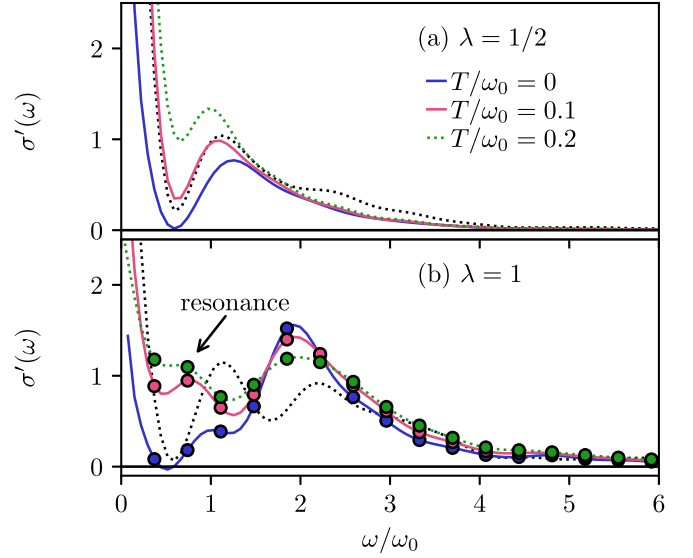

FIG. 13. (a) Optical conductivity for the Holstein bipolaron for $\lambda = 1/2$, $L = 20$, $M = 20$ and $t_{\mathrm{ph}}/\omega_0 = 0$. The black dotted line is the polaron curve with $\lambda = 1/2$, $T = 0.1$, $\epsilon_{\mathrm{bond}} = \epsilon_{\mathrm{LBO}} = 10^{-9}$ and scaled with a factor of two. (b) Same as (a) but with $\lambda = 1$. We use $\epsilon_{\mathrm{bond}} = 5 \times 10^{-9}$, $\epsilon_{\mathrm{LBO}} = 10^{-9}$ for the ground-state data and $\epsilon_{\mathrm{bond}} = 5 \times 10^{-9}$, $\epsilon_{\mathrm{LBO}} = 10^{-8}$ for the finite-temperature data. The symbols show the data points without zero padding. We time evolve to $t_{\mathrm{max}}\omega_0 = 8.5$ and use a Gaussian broadening with $\eta = 0.2/(4\pi)$. The black dotted line in (b) is the polaron curve with $\lambda = 1$, $T = 0.1$, $\epsilon_{\mathrm{bond}} = 5 \times 10^{-9}$, $\epsilon_{\mathrm{LBO}} = 10^{-9}$ and scaled with a factor of two. The simulations are done with p2TDVP-LBO and are distributed onto four processes for the ground-state calculations and onto (ten) eight processes for the (bi)polaron finite-temperature calculations.

substantial differences in the spectrum between both the two different electron-phonon coupling parameters, as well as between the polaron and bipolaron for $\lambda = 1$. For $\lambda = 1/2$, see Fig. 13(a), the bipolaron spectrum is almost identical to the single-polaron spectrum weighted by a factor of two. When $\lambda = 1$, we obtain quite a different picture. Whereas the $\omega/\omega_0 = 1$, 2 peaks have a similar amplitude for the polaron when $t_{\mathrm{ph}}/\omega_0 = 0$, see Fig. 11(b), the bipolaron has a clear maximum around $\omega/\omega_0 = 2$. This indicates that the two-phonon emission process plays a much more dominant role than for the polaron. As T/ω_0 is increased, a resonance appears that can be distinguished from the rest of the spectrum [indicated by the arrow in Fig. 13(b)]. We believe that this stems from the enhanced importance of the one phonon emission peak, which shifts to lower frequencies, similar to what can be seen in Fig. 13(a). When the temperature is increased, the two electrons act more like separate polarons, and the one-phonon emission process becomes more important (for very high temperatures, the bipolaron will dissolve).

We want to emphasize that we focus on the single-bipolaron limit to properly understand the behavior in a dilute system. This is also motivated by the recent results on bipolaron high-temperature superconductivity reported in Ref. [16]. Going to a finite bipolaron density will add scattering, whose effects are beyond the scope of our study. We also observe that when we increase the density to two spinless electrons, the spectrum does practically not change compared
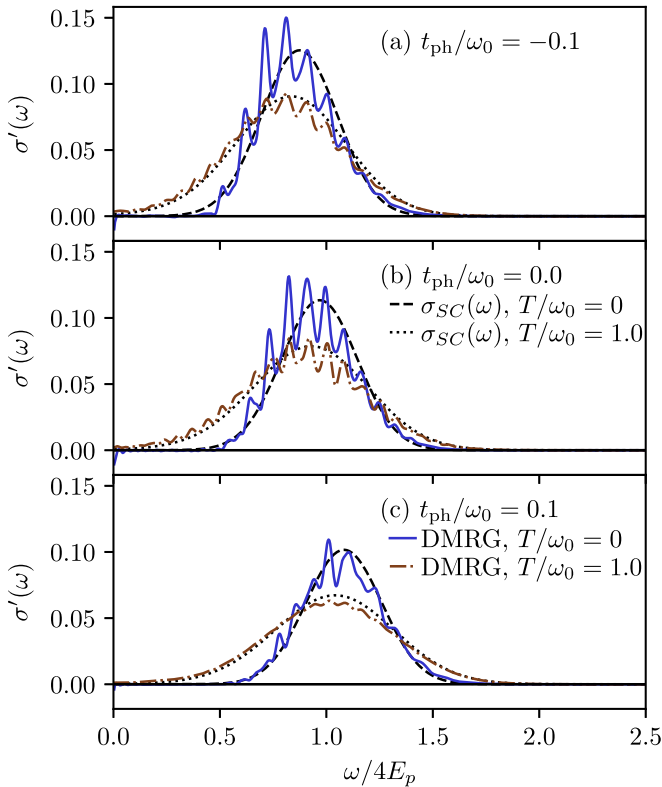
FIG. 14. (a) Optical conductivity for the Holstein bipolaron with $\lambda = 4$ and $t_{\mathrm{ph}}/\omega_0 = -0.1$. (b) Same as in (a) but with $t_{\mathrm{ph}}/\omega_0 = 0$. (c) Same as in (a) but with $t_{\mathrm{ph}}/\omega_0 = 0.1$. We further set $M = 35$, $L = 20$, and $\epsilon_{\mathrm{Bond}} = \epsilon_{\mathrm{LBO}} = 10^{-7}$ for the ground-state calculations. For the time evolution for $T/\omega_0 = 1.0$, we use single-site TDVP with $\epsilon_{\mathrm{bond},J} = 10^{-7}$ for $t_{\mathrm{ph}}/\omega_0 = -0.1, 0.1$ and $\epsilon_{\mathrm{bond},J} = 10^{-8}$ for $t_{\mathrm{ph}}/\omega_0 = 0$ (see Sec. IV for details). The time-evolution is done up to $t_{\max}\omega_0 = 11$ and we use a Gaussian broadening with $\eta = 0.2/(4\pi)$. The dashed and dotted black lines are the analytical formula from Eq. (16). The ground-state simulations are done with p2TDVP-LBO and distributed onto four processes.

to the single electron case (except for a rescaling with a factor of two). This indicates that the change in the spectrum in Fig. 13(b) can be attributed to the formation of a bound bipolaron and not to the change in density. In Fig. 13(b), we also show the data points without zero padding to illustrate that the resonance is not an artifact of the Fourier transformation. While not shown here, we additionally confirmed that the ground-state data in Fig. 13 and data obtained with the Lanczos method agree, as we illustrate for the polaron in Sec. V.

In Fig. 14, we display the real part of the optical conductivity in the strong-coupling regime ($\lambda = 4$). The first key observation is that the analytical formula in Eq. (16) is qualitatively consistent with the DMRG data. An asymmetric Gaussian with a dispersion-dependent maximum (around $4E_P$ for $t_{\mathrm{ph}}/\omega_0 = 0$) is seen in both cases. For $T/\omega_0 = 1$, the maximum is shifted to smaller frequencies and substantial spectral weight can be observed at small ω. This is similar to what occurred for the polaron, see Fig. 12, although a clear dispersion dependence on the low-frequency weight can not be identified for the parameters chosen here. Still, we conclude that Eq. (16) also describes the real part of the optical

conductivity for the bound bipolaron quantitatively well. We note that we can still detect small finite-size effects in some of the oscillation amplitudes in Fig. 14. This is further discussed in Appendix B.

VIII. CONCLUSION

In this work, we tackled the challenging task of accurately computing finite-temperature transport properties in polaron systems. We used single-site TDVP and two-site serial and parallel TDVP combined with local basis optimizations to calculate the real part of the optical conductivity for the Holstein polaron and bipolaron models with dispersive phonons at finite temperatures. We first explained how we incorporate LBO into two-site TDVP and reviewed the key ideas of the parallel implementation. The implementation of p2TDVP gives us the possibility to distribute the system onto different processes, thus allowing for an efficient time evolution while taking advantage of modern computer architectures. This, combined with LBO, allows us to compute time-dependent correlation functions for electron-phonon (bi)polaron systems with a variety of electron-phonon interaction strengths.

We first verified that the results obtained with p2TDVP are consistent with those calculated with the Lanczos method for the ground state of the Holstein polaron. We observed that even a small but finite phonon bandwidth has a significant impact on the optical conductivity for weak and intermediate electron-phonon coupling, consistent with previously reported results [36]. Most importantly, our method can accurately reproduce the Lanczos method data. For strong electron-phonon coupling, the known result of an asymmetric Gaussian is reproduced for $t_{\mathrm{ph}}/\omega_0 = 0$. However, a finite bandwidth shifts the center of the Gaussian to higher or lower frequencies depending on the sign of the phonon hopping amplitude t_{ph}. This can be understood by inspecting the Born-Oppenheimer surfaces of the Holstein dimer as we saw in Sec. III.

Going to finite temperatures significantly alters the optical conductivity. For weak electron-phonon coupling, an increase of spectral weight around $\omega/\omega_0 = 1$ appears. Furthermore, the previously clearly distinguishable peaks almost completely merge at $t_{\mathrm{ph}}/\omega_0 = 0.1$.

For intermediate electron-phonon coupling, the separated peaks remain distinguishable for $t_{\mathrm{ph}}/\omega_0 = 0, 0.1$, whereas the finite temperatures analyzed here do not alter the spectrum much for $t_{\mathrm{ph}}/\omega_0 = -0.1$. In the large coupling case, our data verify the validity for Eq. (16) in the nonadiabatic regime. For $T/\omega_0 = 1$, the maximum of the Gaussian-shaped curve, compared to the $T/\omega_0 = 0$ case, shifts to smaller frequencies, and significant spectral weight is seen at lower frequencies. This is more prominent for an upwards than for a downwards phonon dispersion relation.

Lastly, we presented results for the bound bipolaron. There, we compared weak and intermediate electron-phonon coupling data for dispersionless phonons. While the real part of the optical conductivity for the first parameter set resembles that of the single polaron, a quite different behavior is seen when $\lambda = 1$. There, the maximum of the spectrum is shifted to $\omega/\omega_0 = 2$, signaling the importance of two-phonon emission processes. These parameters also give rise to a large distinguishable peak at small frequencies. Our strong-coupling

bipolaron data reproduce the analytic predictions drawn from the analysis of the Born-Oppenheimer surfaces very well. We reported a dispersion-dependent shift of the maximum of the spectrum and a significant decrease in the amplitude for $T/\omega_0 = 1$, in comparison to the zero-T results. Furthermore, there is enhanced spectral weight for low frequencies.

These results characterize how the main features of small and large polarons in a Holstein-type system change under phonon dispersion and at finite temperatures. Understanding the basic mechanisms in such theoretical Hamiltonians constitutes an essential step in detecting such features, or lack thereof, in experimental data.

There are many interesting extensions to this work. For one, our numerical method can suffer from low-frequency resolution due to the limitations in reachable times. This could lead to small distinct features of the optical conductivity not being detected. Furthermore, despite the benefits of using LBO, there will always be a limit set by phonon truncation. For this reason, one goal of this work is to provide reliable data in the regimes where DMRG is the most powerful (intermediate electron-phonon interaction) which is out of reach of perturbative methods, see, e.g., Ref. [125]. These can then be used to reliably benchmark results obtained with other methods, see, e.g., Refs. [126–135], which might have their strong suit in complementary parameter regimes.

Additionally, including electron-electron interactions in the Born-Oppenheimer formalism can lead to new insights into the transition from bound to unbound bipolarons [44–48,51,53,54]. As this can involve additional numerical complexity, it can also serve as an interesting future application for the methods presented here.

Furthermore, one could try to compare the computations with other finite-temperature matrix-product state methods such as minimally entangled typical thermal state algorithms (METTS), see, e.g., Refs. [79,101,102].

Lastly, an interesting application for our method would be to calculate properties for more complicated Hamiltonians, such as those inspired by manganite physics, see, e.g., Ref. [136] for a theoretical review.

The code and the numerical data in the figures are partially available [137].

APPENDIX A: BOND AND LOCAL BASIS DIMENSIONS

We here discuss the numerical details of the p2TDVP-LBO algorithm. In Fig. 15, we compare how the computation of the
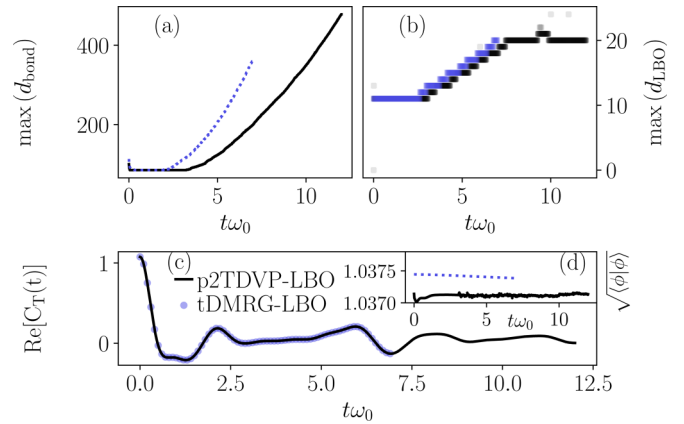

FIG. 15. (a) Maximum bond dimension of the matrix-product state at finite temperature after applying the current operator during the real-time evolution. We use with $\gamma/\omega_0 = \sqrt{2}$, $t_{\text{ph}}/\omega_0 = 0.1$, $M = 20$, $L = 20$, and $\epsilon_{\text{Bond}} = \epsilon_{\text{LBO}} = 10^{-9}$. The time-evolution methods are tDMRG-LBO and p2TDVP-LBO, see Appendix A for details. (b) Maximum local optimal basis dimension after the SVD in the time evolution algorithms (step two for p2TDVP-LBO and see Ref. [35] for details for the tDMRG-LBO algorithm). (c) Real part of the current-current correlation function. (d) Norm of the initial state. (b)–(d) have the same parameters as (a).

current-current correlation functions scales compared to the tDMRG-LBO algorithm applied in Ref. [35]. Note that we use tDMRG-LBO to obtain the thermal state with imaginary-time evolution and to do the real-time evolution shown in Fig. 15. The agreement between the two methods seen in Fig. 15(c) serves as a check for our p2TDVP-LBO algorithm. As explained in Sec. IV, the real-time evolution is carried out on the state $|\phi_T\rangle = \hat{J} |\psi_T\rangle$. In Fig. 15(a), we show the maximum bond dimension of $|\phi_T\rangle$ as a function of time with $\epsilon_{\text{Bond}} = \epsilon_{\text{LBO}} = 10^{-9}$ for both time-evolution methods. The need for a smaller bond dimension for p2TDVP is apparent, consistent with previous benchmarks of MPS time-evolution algorithms [81]. Figure 15(b) displays the maximum LBO dimension used in the SVD after applying the time-evolution gate in the tDMRG-LBO algorithm and step two of the p2TDVP-LBO algorithm (see Sec. IV for details). In both cases, using LBO is beneficial for the parameters chosen here. In Fig. 15(d), we plot the norm of the state $|\phi_T\rangle$. Note that $\sqrt{\langle\phi_T | \phi_T\rangle} \neq 1$ since we already applied $\hat{J}$. The initial norm deviates between the two methods since the initial states are obtained using the different time-evolution schemes. Neither norm changes significantly during the reachable times. The reason why the time evolution is carried out until different times is the difference in computational cost. Note that this analysis does not account for the advantage of being able to distribute the computations onto several processes in the p2TDVP-LBO algorithm.

We now demonstrate that the calculations of the correlation function at finite temperatures can be homogeneously distributed onto several processes. In Fig. 16, we show that the bond dimension is roughly equal on all the bonds at different times for the bulk of the system. There, we plot the bond dimension between the different sites at the times $t\omega_0 = 8$, 12, and 13 for the Holstein polaron. The parameters are given in the caption of Fig. 16. Furthermore, the grey dashed lines show where the partitioning of the
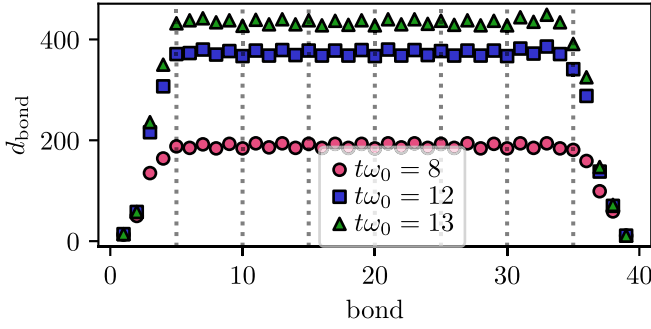
FIG. 16. Bond dimension between different sites at different times for the matrix-product state $|\phi_T\rangle$ for the Holstein polaron during time-evolution with p2TDVP-LBO. The calculations are done at the temperature $T/\omega_0 = 0.2$ and with the parameters $\lambda = 1$, $t_{\mathrm{ph}}/\omega_0 = 0.1$, $M = 20$, $L = 20$, $\epsilon_{\mathrm{bond}} = 5 \times 10^{-9}$, and $\epsilon_{\mathrm{LBO}} = 10^{-9}$. The dashed vertical lines show the partitioning of the system onto eight processes.

system is done. Therefore, a need for dynamically adapting the boundaries as suggested for pDMRG in Ref. [138] does not seem necessary for our applications.

Lastly, in our discussion of the numerical details of p2TDVP-LBO, we illustrate the difference between using a regular Krylov solver, a Krylov solver with LBO (Krylov-LBO), and RK4 with LBO (RK4-LBO) in step one of the algorithm (see Sec. IV for details). In our test case, we apply the three versions of the algorithm to the real-time evolution of the bipolaron ground state after applying the current operator $|\phi_0\rangle = \hat{J}|\psi_0\rangle$. Note that the results, as in all LBO calculations, will be system and set-up dependent and a benchmark should be carried out in each case separately when feasible.

Figure 17(a) shows the average CPU time for each time step with the three methods. One first observes that the exponential increase in the bond dimension dominates the computation time in all cases. Still, using Krylov-LBO seems to be faster than using the regular Krylov solver. The RK4-LBO algorithm is significantly faster for the times reached here. We believe that this can be understood as follows: The Krylov vectors for a general state $|\psi\rangle$, are $|\psi\rangle_0 = |\psi\rangle$, $|\psi\rangle_1 = \hat{H}|\psi\rangle_0$, $|\psi\rangle_2 = \hat{H}|\psi\rangle_1 = \hat{H}^2|\psi\rangle_0$, and so on. The LBO basis is found before $\hat{H}$ is applied. Through the polynomial application of $\hat{H}$, we expect a larger phonon Hilbert space to be explored, which requires a larger number of LBO states. However, for the RK4 algorithm, $|k^1\rangle = \hat{H}|\psi\rangle$, but $|k^2\rangle = \hat{H}(|\psi\rangle + \alpha dt |k^1\rangle) = (\hat{H}|\psi\rangle + \alpha dt \hat{H}^2 |\psi\rangle)$ etc, where α is a number. Now, the term including $\hat{H}^2$ is scaled with dt. We thus believe that for small dt, the optimal basis changes less drastically than for the Krylov vector $|\psi\rangle_2$. This seems plausible when inspecting the LBO dimensions needed in the calculations.

In Fig. 17(b), we show the maximum LBO dimension needed in the different algorithms. The red dotted line are the maximum LBO dimension used in the Krylov-LBO steps whereas the light red dotted line is the average. The maximum LBO dimension in the Krylov algorithm quickly reaches the maximum, which we already attributed to the fact that one must apply the effective Hamiltonian several times. The average remains somewhat lower. The required LBO dimension
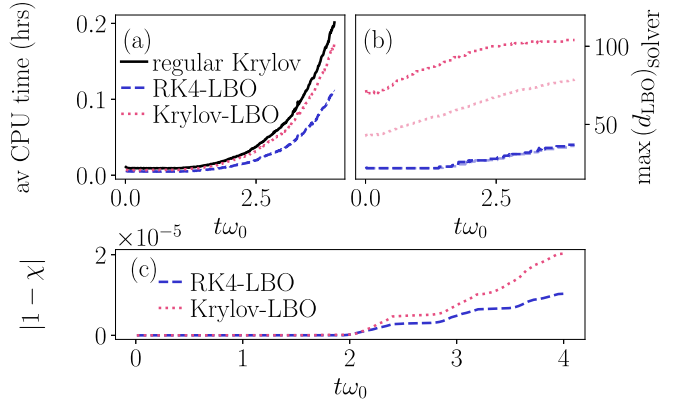

FIG. 17. Different local basis optimization schemes for two-site TDVP when calculating the real-time evolution of the bipolaron ground state after applying the current operator. The parameters are $L = 13$, $M = 25$, $\gamma/\omega_0 = 1$, $t_{\mathrm{ph}}/\omega_0 = 0.0$, and $\epsilon_{\mathrm{bond}} = \epsilon_{\mathrm{LBO}} = 10^{-9}$. (a) Average CPU time for the different implementations in step one of the two-site TDVP algorithm, see Sec. IV for details. Black solid line: regular Krylov solver. Red dotted line: Krylov-LBO. Blue dashed line: RK4-LBO. (b) Maximum optimal basis dimension in the two-site TDVP with the Krylov-LBO (red dotted line) and with the RK4-LBO (blue dashed line) solver. The light lines are calculated by averaging the LBO dimension in all the Krylov vectors or all the k^j in the RK4 algorithm, and then taking the maximum of all the sites. (c) Absolute value of the overlap $\chi - 1$ of the wave function with a LBO solver and with the regular Krylov solver. Red dotted line: Krylov-LBO. Blue dashed line: RK4-LBO. All simulations use two cores.

is significantly smaller in RK4-LBO (the average and maximum almost perfectly overlap), making the algorithm more efficient.

We also observe that the difference between RK4-LBO and Krylov-LBO is negligible for the time scales studied here. Figure 17(c) shows the absolute value of $1 - \chi$, where χ is the overlap between either the state using Krylov-LBO (red dotted line) or RK4-LBO (blue dashed line) with the state which uses a Krylov method without LBO. The difference is small for all times in our test case. We further want to point out that the RK4 solver, in general, is not as stable as the Krylov solver. For example, it did not converge well for the imaginary-time evolution in our calculations (which is why we use the regular Krylov solver in that case). For that reason, we also compared our results computed with the RK4-LBO solver to those obtained with a Krylov solver without LBO.

APPENDIX B: COMPARING THE MOMENTS

We now want to estimate the accuracy of the Fourier transform of the time-evolved current-current correlation function, see Eq. (8), which we use to extract $\sigma'(\omega)$. To do that, we compare the moments of the correlation function calculated in two ways: by calculating a thermal expectation value of the initial state and integrating the correlation function over ω. Computing the moments to assess the accuracy of the calculations for the Holstein polaron has already been used for the spectral functions, see, e.g., Refs. [33,35,139,140]. We

define the kth moment to be

$$\tilde{M}_k = \int_{-\infty}^{\infty} d\omega (\omega)^k C(\omega)_T. \tag{B1}$$

The zeroth moment is then

$$\tilde{M}_0 = \int_{-\infty}^{\infty} d\omega C(\omega)_T = \pi \langle \hat{J}^2 \rangle_T. \tag{B2}$$

The first moment becomes

$$\tilde{M}_1 = \int_{-\infty}^{\infty} d\omega \omega C(\omega)_T = \pi \langle [\hat{J}, \hat{H}] \hat{J} \rangle_T, \tag{B3}$$

where $[\hat{J}, \hat{H}] = [\hat{J}, \hat{H}_{\text{kin}}] + [\hat{J}, \hat{H}_{\text{e-ph}}]$ with

$$[\hat{J}, \hat{H}_{\text{kin}}] = -it_0^2 \sum_s (2\hat{c}_{1,s}^\dagger \hat{c}_{1,s} - 2\hat{c}_{L,s}^\dagger \hat{c}_{L,s}) \tag{B4}$$

and

$$[\hat{J}, \hat{H}_{\text{e-ph}}] = \gamma t_0 i \left(\sum_{j=2,s}^{L} (\hat{c}_{j-1,s}^\dagger \hat{c}_{j,s} + \hat{c}_j^\dagger \hat{c}_{j-1,s})(\hat{b}_j^\dagger + \hat{b}_j) \right.$$
$$\left. - \sum_{j=1,s}^{L-1} (\hat{c}_{j,s}^\dagger \hat{c}_{j+1,s} + \hat{c}_{j+1,s}^\dagger \hat{c}_{j,s})(\hat{b}_j^\dagger + \hat{b}_j) \right). \tag{B5}$$

Lastly, the second moment becomes

$$\tilde{M}_2 = \int_{-\infty}^{\infty} d\omega \omega^2 C(\omega)_T = \pi \langle [[\hat{J}, \hat{H}], \hat{H}] \hat{J} \rangle_T, \tag{B6}$$

with

$$[[\hat{J}, \hat{H}], \hat{H}] = it_0^3 2 \left(\sum_{s=\uparrow,\downarrow} \left(\hat{c}_{1,s}^\dagger \hat{c}_{2,s} - \hat{c}_{2,s}^\dagger \hat{c}_{1,s} \right. \right.$$
$$\left. + \hat{c}_{L-1,s}^\dagger \hat{c}_{L,s}^\dagger - \hat{c}_{L,s}^\dagger \hat{c}_{L-1,s} \right) \Big)$$
$$+ \gamma t_0 \omega_0 i \left(\sum_{j=2,s=\uparrow,\downarrow}^{L} \left(\hat{c}_{j-1,s}^\dagger \hat{c}_{j,s} \hat{b}_j + \hat{c}_{j,s}^\dagger \hat{c}_{j-1,s} \hat{b}_j \right. \right.$$
$$\left. - \hat{c}_{j-1,s}^\dagger \hat{c}_{j,s} \hat{b}_j^\dagger - \hat{c}_{j,s}^\dagger \hat{c}_{j-1,s} \hat{b}_j^\dagger \right)$$
$$+ \sum_{j=1,s=\uparrow,\downarrow}^{L-1} \left(-\hat{c}_{j,s}^\dagger \hat{c}_{j+1,s} \hat{b}_j - \hat{c}_{j+1,s}^\dagger \hat{c}_{j,s} \hat{b}_j \right.$$
$$\left. + \hat{c}_{j,s}^\dagger \hat{c}_{j+1,s} \hat{b}_j^\dagger + \hat{c}_{j+1,s}^\dagger \hat{c}_{j,s} \hat{b}_j^\dagger \right) \Big)$$
$$+ it_0 \gamma t_{\text{ph}} \left(\sum_{j=2,s=\uparrow,\downarrow}^{L-1} \left(\hat{c}_{j-1,s}^\dagger \hat{c}_j \hat{b}_{j+1} + \hat{c}_{j,s}^\dagger \hat{c}_{j-1,s} \hat{b}_{j+1} \right. \right.$$
$$\left. - \hat{c}_{j-1,s}^\dagger \hat{c}_{j,s} \hat{b}_{j+1}^\dagger - \hat{c}_{j,s}^\dagger \hat{c}_{j-1,s} \hat{b}_{j+1}^\dagger \right) \Big)$$
$$- it_0 \gamma t_{\text{ph}} \left(\sum_{j=2,s=\uparrow,\downarrow}^{L-1} \left(\hat{c}_{j,s}^\dagger \hat{c}_{j+1,s} \hat{b}_j + \hat{c}_{j+1,s}^\dagger \hat{c}_{j,s} \hat{b}_j \right. \right.$$
$$\left. - \hat{c}_{j,s}^\dagger \hat{c}_{j+1,s} \hat{b}_j^\dagger - \hat{c}_{j+1,s}^\dagger \hat{c}_{j,s} \hat{b}_j^\dagger \right) \Big)$$

$$- it_0 \gamma^2 \left(\sum_{j=1,s=\uparrow,\downarrow}^{L-1} \left(\hat{c}_{j+1,s}^\dagger \hat{c}_{j,s} (\hat{X}_j)^2 \right. \right.$$
$$- \hat{c}_{j+1,s}^\dagger \hat{c}_{j,s} \hat{X}_j \hat{X}_{j+1}$$
$$\left. + \hat{c}_{j,s}^\dagger \hat{c}_{j+1,s} \hat{X}_j \hat{X}_{j+1} - \hat{c}_{j,s}^\dagger \hat{c}_{j+1,s} (\hat{X}_j)^2 \right) \Big)$$
$$+ it_0 \gamma^2 \left(\sum_{j=2,s=\uparrow,\downarrow}^{L} \left(\hat{c}_{j-1,s}^\dagger \hat{c}_{j,s} (\hat{X}_j)^2 - \hat{c}_{j-1,,s}^\dagger \hat{c}_{j,s} \hat{X}_j \hat{X}_{j-1} \right. \right.$$
$$\left. + \hat{c}_{j,s}^\dagger \hat{c}_{j-1,s} \hat{X}_j \hat{X}_{j-1} - \hat{c}_{j,s}^\dagger \hat{c}_{j-1,s} (\hat{X}_j)^2 \right) \Big)$$
$$- \gamma t_0^2 i \left(\sum_{j=1,s=\uparrow,\downarrow}^{L-2} \left(\hat{c}_{j+2,s}^\dagger \hat{c}_{j,s} - \hat{c}_{j,s}^\dagger \hat{c}_{j+2,s} \right) \hat{X}_j \right.$$
$$\left. + \sum_{j=1,s=\uparrow,\downarrow}^{L-2} \left(\hat{c}_{j,s}^\dagger \hat{c}_{j+2,s} - \hat{c}_{j+2,s}^\dagger \hat{c}_{j,s} \right) \hat{X}_{j+1} \right)$$
$$- \gamma t_0^2 i \left(\sum_{j=2}^{L-1} \left(\hat{c}_{j-1,s}^\dagger \hat{c}_{j+1,s} - \hat{c}_{j+1,s}^\dagger \hat{c}_{j-1,s} \right) X_j \right.$$
$$\left. + \sum_{j=2,s=\uparrow,\downarrow}^{L-1} \left(\hat{c}_{j+1,s}^\dagger \hat{c}_{j-1,s} - \hat{c}_{j-1,s}^\dagger \hat{c}_{j+1,s} \right) \hat{X}_{j+1} \right), \tag{B7}$$

with $\hat{X}_i = \hat{b}_i^\dagger + \hat{b}_i$. Figure 18 shows $\tilde{M}_1$, $\tilde{M}_2$, and $\tilde{M}_3$ for the same data as plotted in Fig. 11. We display both the integrated correlation functions (integrated for $\omega/\omega_0 \in [-15, 15]$) and the thermal expectation values. The relative difference is at maximum of the order of $\mathcal{O}(10^{-3})$. For the data shown in Fig. 10, the relative difference is also at maximum of the order of $\mathcal{O}(10^{-3})$. The moments without zero padding are in some cases just as good as for the data with zero padding. For the DMRG data in Fig. 12, we integrated for $\omega/\omega_0 \in [-80, 80]$ and obtain a relative difference at maximum of the order $\mathcal{O}(10^{-3})$. For the bipolaron data in Fig. 13, the difference in the moments are at most of the order $\mathcal{O}(10^{-3})$ when integrated for $\omega/\omega_0 \in [-15, 15]$. In Fig. 14, the relative difference is of order $\mathcal{O}(10^{-3})$ when we integrate for $\omega/\omega_0 \in [-50, 50]$.

To quantify the influence of the phonon cutoff M for large coupling and large temperatures ($T/\omega_0 = 1$), we compare several quantities in Fig. 19. Figure 19(a) shows the relative difference in the f-sum rule between the initial state and the integrated real part of the optical conductivity:

$$d(\text{f-sum}) = \frac{\left| \int_0^\infty d\omega \sigma'(\omega) - \frac{-\pi \langle E_{\text{kin}} \rangle_T}{2} \right|}{\left| \frac{-\pi \langle E_{\text{kin}} \rangle_T}{2} \right|}. \tag{B8}$$

Note that all terms in Eq. (B8) are evaluated with the same phonon truncation M and that we integrate for $\omega/\omega_0 \in [0, 80]$. We observe that the result improves as M is increased. The empty symbols show the same data but without zero padding. As can be seen, the sparse number of integration points produces inaccurate results. We also mention that the type of methods used has difficulties correctly capturing the low-frequency physics due to the limitations in reachable times.
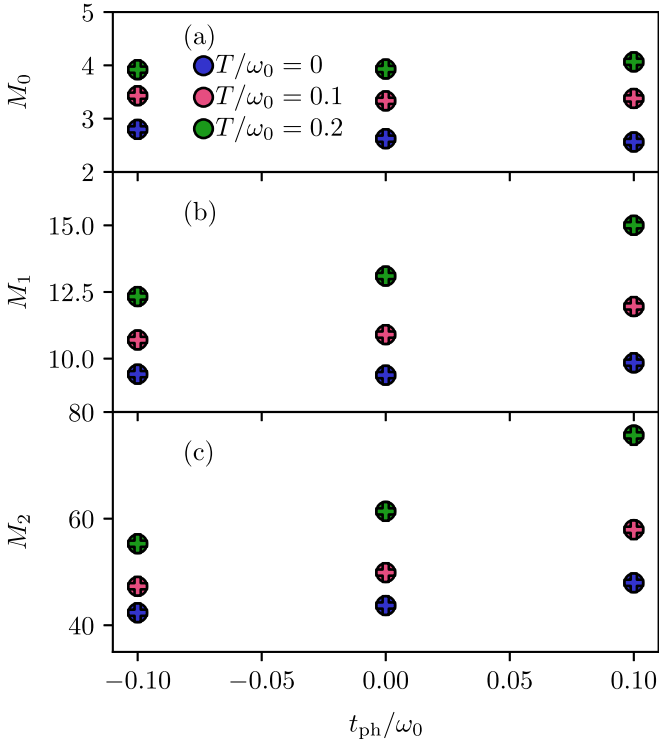
FIG. 18. Moments of the correlation function for the same parameters as in Fig. 11. (a) Zeroth moment, (b) first moment, (c) second moment. The circles are calculated by integrating the Fourier transformed data obtained with time evolution and the plus signs from evaluating the commutators at finite temperatures. For details, see Appendix B.

This can also lead to inaccurate results for the f-sums rule, in particular for systems with a significant Drude weight. In Fig. 19(b), we illustrate how the moments behave when M is varied. There, we show the relative difference between the integral over the correlation function (integrated for $\omega/\omega_0 \in [-80, 80]$) and the thermal expectation value (i.e., right-hand side of Eq. (B2) for $\tilde{M}_0$) denoted as $\langle \hat{\tilde{M}}_k \rangle_T$:

$$d(\tilde{M}_k) = \frac{\left| \int_{-\infty}^{\infty} d\omega (\omega)^k C(\omega)_T - \langle \hat{\tilde{M}}_k \rangle_T \right|}{|\langle \hat{\tilde{M}}_k \rangle_T|}. \quad \text{(B9)}$$

We first see that all moments have similar accuracy. Still, while not shown here, the moments do seem to converge individually when M is increased. We wish to emphasize that the moments are very accurate with and without zero padding and thus must be used with caution as convergence criteria.

One sees the influence of the different M on the optical conductivity in Fig. 19(c). Even for the largest M used here, small differences in some of the peak amplitudes can be observed. Still, the spectrum is quantitatively well captured. We also want to note that the real part of the optical conductivity in Fig. 19(c) has an η dependence as well. This can be understood by inspecting the current-current correlation function (not shown here). There are still some M dependent oscillations at longer times which get suppressed when η is large. This is not the case for $t_{\text{ph}}/\omega_0 \neq 0$, where the correlation functions have no notable oscillations for large times t/ω_0. Similar behavior is seen for the ground-state calculations in
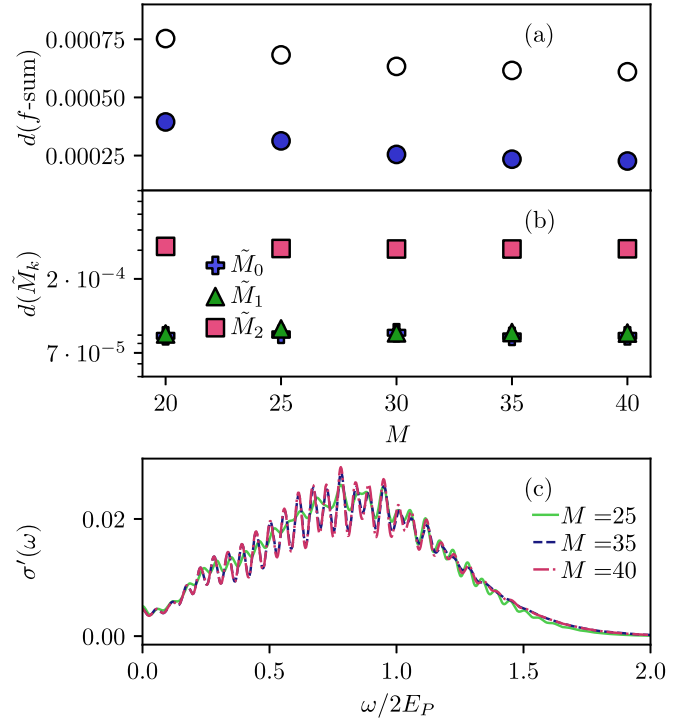

FIG. 19. (a) Relative difference in the f-sum rule, see Appendix B for details. (b) Relative difference in the moments, also see Appendix B. (c) Real part of the optical conductivity. All data are at $T/\omega_0 = 1$ and with different phonon cutoff M. The rest of the parameters are the same as in Fig. 12. The open circles in (a) show the data when no zero padding is used.

Fig. 9. In some cases, we also observe some L dependence in the amplitudes of the optical conductivities. This is illustrated in Fig. 20.

We further want to remark that the use of zero padding is not strictly necessary when using single-site TDVP as is done for $T/\omega_0 = 1$. This is because the computational cost does not increase with time. However, we do this to justifiably compare it to the ground-state data, for which we use p2TDVP-LBO, and which has an increased computational cost with time. We can conclude that for our data, the convergence of the integral and the expectation values is a necessary but not a sufficient criterion to ensure proper convergence of the optical conductivity for parameters of the initial state. The convergence of the moments relative to each other seems to work better.

Furthermore, the moments and the kinetic energy are used to ensure that the initial thermal state is converged with respect to ρ_{LBO}, ρ_{bond}, M, and the imaginary-time step. The largest relative difference is of order $\mathcal{O}(10^{-3})$ and is found for some quantities for the large coupling polaron and bipolaron at $T/\omega_0 = 1$. We also computed the relative overlap between states with different ρ_{LBO}, ρ_{bond} and imaginary time steps and found a maximum difference from one of the order of $\mathcal{O}(10^{-5})$ for strong coupling and $T/\omega_0 = 1.0$ and $\mathcal{O}(10^{-6})$ for the rest of our finite T/ω_0 data.

APPENDIX C: BORN-OPPENHEIMER SURFACES

In order to derive an analytic expression for the real part of the optical conductivity for strong electron-phonon coupling,
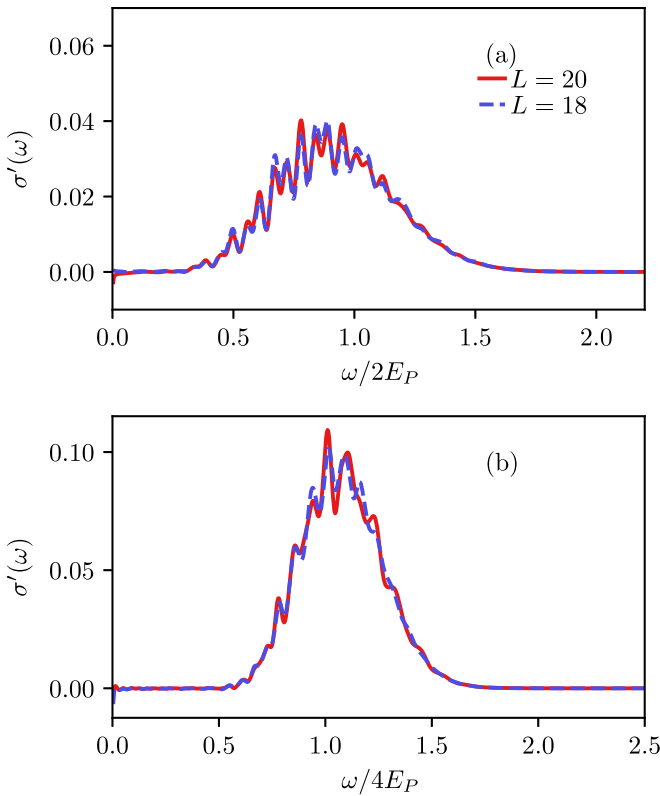
FIG. 20. (a) Ground-state optical conductivity for the polaron from Fig. 12(b) for two different system sizes. All other parameters are the same as in Fig. 12(b). (b) Ground-state optical conductivity for the bipolaron from Fig. 14(c) for the same system sizes as in (a). All other parameters are the same as in Fig. 14(c).

we first obtain the Born-Oppenheimer Hamiltonian [91,92] from Eq. (15). For a fixed $\bar{q}$ this becomes a 2×2 matrix, in the polaron case, which can be diagonalized

$$H_{\mathrm{BO}} = \begin{pmatrix} \frac{\bar{q}^2}{2}\tilde{\omega}_0 + \gamma\bar{q} & -t_0 \\ -t_0 & \frac{\bar{q}^2}{2}\tilde{\omega}_0 - \gamma\bar{q} \end{pmatrix}, \qquad \text{(C1)}$$

where $\tilde{\omega}_0 = \omega_0 - t_{\mathrm{ph}}$. The Hamiltonian has the energies $E_{\pm}^{\mathrm{BO}} = \frac{1}{2}(\bar{q}^2\tilde{\omega}_0 \pm 2\sqrt{(\gamma\bar{q})^2 + t_0^2})$. These energies give the Born-Oppenheimer surfaces. Their extrema with respect to $\bar{q}$ can be found by setting their derivatives to zero and one obtains $\bar{q} = 0$, and $\bar{q}_{\mathrm{min},\pm} = \pm\frac{\sqrt{\gamma^4 - \tilde{\omega}_0^2 t_0^2}}{\tilde{\omega}_0\gamma}$. The Born-Oppenheimer surfaces can be seen in Fig. 2(a) for different phonon dispersion relations. The minima of the lower surface decrease as the phonon hopping goes from $t_{\mathrm{ph}}/\omega_0 = -0.1$ to $+0.1$. We obtain $\Delta^{\mathrm{BO}} = E_+^{\mathrm{BO}}(q_{\mathrm{min},\pm}) - E_-^{\mathrm{BO}}(q_{\mathrm{min},\pm}) = 2\sqrt{\frac{\gamma^4 - \tilde{\omega}_0^2 t_0^2}{\tilde{\omega}_0^2} + t_0^2}$. For the bipolaron, we have a 4×4 matrix

$$H_{\mathrm{BO}} = \begin{pmatrix} \frac{\bar{q}^2}{2}\tilde{\omega}_0 + 2\gamma\bar{q} & -t_0 & -t_0 & 0 \\ -t_0 & \frac{\bar{q}^2}{2}\tilde{\omega}_0 & 0 & -t_0 \\ -t_0 & 0 & \frac{\bar{q}^2}{2}\tilde{\omega}_0 & -t_0 \\ 0 & -t_0 & -t_0 & \frac{\bar{q}^2}{2}\tilde{\omega}_0 - 2\gamma\bar{q} \end{pmatrix}, \qquad \text{(C2)}$$

using the convention $|\uparrow\downarrow, 0\rangle, |\uparrow, \downarrow\rangle, |\downarrow, \uparrow\rangle, |0, \uparrow\downarrow\rangle$ for the electron occupation basis. Here, the surfaces are obtained by solving for the eigenvalues numerically.

To obtain Eq. (16), one uses the fact that the current operator connects the lowest and the first excited surfaces for a fixed $\bar{q}$. To calculate the current-current correlation function, one must then compute [141]

$$\langle e^{i\hat{H}_g t} e^{-i\hat{H}_e t}\rangle_T = \langle e^{-\hat{S}} e^{\hat{S}} e^{i\hat{H}_g t} e^{-\hat{S}} e^{\hat{S}} e^{-i\hat{H}_e t} e^{-\hat{S}} e^{\hat{S}}\rangle_T$$
$$= \langle e^{i\hat{H}_e t} e^{\hat{S}} e^{-i\hat{H}_e t} e^{-\hat{S}}\rangle_T = \langle e^{\hat{S}(t)} e^{-\hat{S}}\rangle_T, \qquad \text{(C3)}$$

where $\hat{H}_g$ is the harmonic oscillator Hamiltonian with frequencies $\tilde{\omega}_0 = \omega_0 - t_{\mathrm{ph}}$ and ladder operators $\hat{a}$ and $\hat{a}^\dagger$. $\hat{H}_e$ is the harmonic oscillator Hamiltonian shifted with the distance d and $e^{-\hat{S}}$ is the Lang-Firsov transformation operator, see Ref. [125], with $\hat{S} = d\sqrt{\frac{1}{2}}(\hat{a} - \hat{a}^\dagger)$. Evaluating Eq. (C3), see, e.g., Ref. [96], rescaling with a factor of two for $L > 2$, and expanding $e^{i\tilde{\omega}_0 t} = 1 + i\tilde{\omega}_0 t - \frac{1}{2}\tilde{\omega}_0^2 t^2 + \mathcal{O}(\tilde{\omega}_0^3)$ before the Fourier transformation leads to Eq. (16).

[1] C. Franchini, M. Reticcioli, M. Setvin, and U. Diebold, Polarons in materials, Nat. Rev. Mater. **6**, 560 (2021).

[2] A. J. Millis, P. B. Littlewood, and B. I. Shraiman, Double Exchange Alone does not Explain the Resistivity of La$_{1-x}$Sr$_x$MnO$_3$, Phys. Rev. Lett. **74**, 5144 (1995).

[3] A. Lanzara, N. L. Saini, M. Brunelli, F. Natali, A. Bianconi, P. G. Radaelli, and S.-W. Cheong, Crossover from Large to Small Polarons across the Metal-Insulator Transition in Manganites, Phys. Rev. Lett. **81**, 878 (1998).

[4] C. Jooss, L. Wu, T. Beetz, R. F. Klie, M. Beleggia, M. A. Schofield, S. Schramm, J. Hoffmann, and Y. Zhu, Polaron melting and ordering as key mechanisms for colossal resistance effects in manganites, Proc. Natl. Acad. Sci. USA **104**, 13597 (2007).

[5] S. Schramm, J. Hoffmann, and C. Jooss, Transport and ordering of polarons in CER manganites PrCaMnO, J. Phys.: Condens. Matter **20**, 395231 (2008).

[6] K. Miyata, D. Meggiolaro, M. T. Trinh, P. P. Joshi, E. Mosconi, S. C. Jones, F. D. Angelis, and X.-Y. Zhu, Large polarons in lead halide perovskites, Sci. Adv. **3**, e1701217 (2017).

[7] D. Cortecchia, J. Yin, A. Bruno, S.-Z. A. Lo, G. G. Gurzadyan, S. Mhaisalkar, J.-L. Brédas, and C. Soci, Polaron self-localization in white-light emitting hybrid perovskites, J. Mater. Chem. C **5**, 2771 (2017).

[8] E. Cinquanta, D. Meggiolaro, S. G. Motti, M. Gandini, M. J. P. Alcocer, Q. A. Akkerman, C. Vozzi, L. Manna, F. De Angelis, A. Petrozza, and S. Stagira, Ultrafast THz Probe of Photoinduced Polarons in Lead-Halide Perovskites, Phys. Rev. Lett. **122**, 166601 (2019).

[9] D. Ghosh, E. Welch, A. J. Neukirch, A. Zakhidov, and S. Tretiak, Polarons in halide perovskites: A perspective, J. Phys. Chem. Lett. **11**, 3271 (2020).

[10] S. Yoon, H. L. Liu, G. Schollerer, S. L. Cooper, P. D. Han, D. A. Payne, S.-W. Cheong, and Z. Fisk, Raman and

optical spectroscopic studies of small-to-large polaron crossover in the perovskite manganese oxides, Phys. Rev. B **58**, 2795 (1998).

[11] M. Quijada, J. Černe, J. R. Simpson, H. D. Drew, K. H. Ahn, A. J. Millis, R. Shreekala, R. Ramesh, M. Rajeswari, and T. Venkatesan, Optical conductivity of manganites: Crossover from Jahn-Teller small polaron to coherent transport in the ferromagnetic state, Phys. Rev. B **58**, 16093 (1998).

[12] S. Mildner, J. Hoffmann, P. E. Blöchl, S. Techert, and C. Jooss, Temperature- and doping-dependent optical absorption in the small-polaron system $Pr_{1-x}Ca_xMnO_3$, Phys. Rev. B **92**, 035145 (2015).

[13] K. H. Kim, J. Y. Gu, H. S. Choi, G. W. Park, and T. W. Noh, Frequency Shifts of the Internal Phonon Modes in $La_{0.7}Ca_{0.3}MnO_3$, Phys. Rev. Lett. **77**, 1877 (1996).

[14] C. Hartinger, F. Mayr, A. Loidl, and T. Kopp, Polaronic excitations in colossal magnetoresistance manganite films, Phys. Rev. B **73**, 024408 (2006).

[15] A. Machida, Y. Moritomo, and A. Nakamura, Spectroscopic evidence for formation of small polarons in doped manganites, Phys. Rev. B **58**, R4281 (1998).

[16] C. Zhang, J. Sous, D. R. Reichman, M. Berciu, A. J. Millis, N. V. Prokof'ev, and B. V. Svistunov, Bipolaronic high-temperature superconductivity, arXiv:2203.07380.

[17] Y. Zhang, T. Kafle, W. You, X. Shi, L. Min, H. (Hugo)Wang, N. Li, V. Gopalan, K. Rossnagel, L. Yang, Z. Mao, R. Nandkishore, H. Kapteyn, and M. Murnane, Bipolaronic nature of the pseudogap in (TaSe4)2I revealed via weak photoexcitation, arXiv:2203.05655.

[18] T. Holstein, Studies of polaron motion: Part I. The molecular-crystal model, Ann. Phys. (NY) **8**, 325 (1959).

[19] R. J. Bursill, R. H. McKenzie, and C. J. Hamer, Phase Diagram of the One-Dimensional Holstein Model of Spinless Fermions, Phys. Rev. Lett. **80**, 5607 (1998).

[20] C. E. Creffield, G. Sangiovanni, and M. Capone, Phonon softening and dispersion in the 1D Holstein model of spinless fermions, Eur. Phys. J. B **44**, 175 (2005).

[21] S. Fratini and S. Ciuchi, Dynamical Mean-Field Theory of Transport of Small Polarons, Phys. Rev. Lett. **91**, 256403 (2003).

[22] O. S. Barišić, Variational study of the Holstein polaron, Phys. Rev. B **65**, 144301 (2002).

[23] O. S. Barišić, Calculation of excited polaron states in the Holstein model, Phys. Rev. B **69**, 064302 (2004).

[24] O. S. Barišić, Holstein light quantum polarons on the one-dimensional lattice, Phys. Rev. B **73**, 214304 (2006).

[25] O. S. Barišić and S. Barišić, Phase diagram of the Holstein polaron in one dimension, Eur. Phys. J. B **64**, 1 (2008).

[26] J. Loos, M. Hohenadler, A. Alvermann, and H. Fehske, Phonon spectral function of the Holstein polaron, J. Phys.: Condens. Matter **18**, 7299 (2006).

[27] J. Loos, M. Hohenadler, and H. Fehske, Spectral functions of the spinless Holstein model, J. Phys.: Condens. Matter **18**, 2453 (2006).

[28] L. Vidmar, J. Bonča, and S. A. Trugman, Emergence of states in the phonon spectral function of the Holstein polaron below and above the one-phonon continuum, Phys. Rev. B **82**, 104304 (2010).

[29] L. Vidmar, J. Bonča, M. Mierzejewski, P. Prelovšek, and S. A. Trugman, Nonequilibrium dynamics of the Holstein polaron

driven by an external electric field, Phys. Rev. B **83**, 134301 (2011).

[30] F. Dorfner, L. Vidmar, C. Brockt, E. Jeckelmann, and F. Heidrich-Meisner, Real-time decay of a highly excited charge carrier in the one-dimensional Holstein model, Phys. Rev. B **91**, 104302 (2015).

[31] C. Brockt and E. Jeckelmann, Scattering of an electronic wave packet by a one-dimensional electron-phonon-coupled structure, Phys. Rev. B **95**, 064309 (2017).

[32] D. Jansen, J. Stolpp, L. Vidmar, and F. Heidrich-Meisner, Eigenstate thermalization and quantum chaos in the Holstein polaron model, Phys. Rev. B **99**, 155130 (2019).

[33] J. Bonča, S. A. Trugman, and M. Berciu, Spectral function of the Holstein polaron at finite temperature, Phys. Rev. B **100**, 094307 (2019).

[34] L. Chen-Yen and S. A. Trugman, Absence of diffusion and fractal geometry in the Holstein model at high temperature, arXiv:2007.00817.

[35] D. Jansen, J. Bonča, and F. Heidrich-Meisner, Finite-temperature density-matrix renormalization group method for electron-phonon systems: Thermodynamics and Holstein-polaron spectral functions, Phys. Rev. B **102**, 165155 (2020).

[36] J. Bonča and S. A. Trugman, Dynamic properties of a polaron coupled to dispersive optical phonons, Phys. Rev. B **103**, 054304 (2021).

[37] E. Jeckelmann, C. Zhang, and S. R. White, Metal-insulator transition in the one-dimensional Holstein model at half filling, Phys. Rev. B **60**, 7950 (1999).

[38] C. Zhang, E. Jeckelmann, and S. R. White, Dynamical properties of the one-dimensional Holstein model, Phys. Rev. B **60**, 14092 (1999).

[39] H. Zhao, C. Q. Wu, and H. Q. Lin, Spectral function of the one-dimensional Holstein model at half filling, Phys. Rev. B **71**, 115201 (2005).

[40] H. Hashimoto and S. Ishihara, Photoinduced charge-order melting dynamics in a one-dimensional interacting Holstein model, Phys. Rev. B **96**, 035154 (2017).

[41] J. Stolpp, J. Herbrych, F. Dorfner, E. Dagotto, and F. Heidrich-Meisner, Charge-density-wave melting in the one-dimensional Holstein model, Phys. Rev. B **101**, 035134 (2020).

[42] M. Weber and J. K. Freericks, Field tuning beyond the heat death of a charge-density-wave chain, arXiv:2107.04096.

[43] D. Jansen, C. Jooss, and F. Heidrich-Meisner, Charge density wave breakdown in a heterostructure with electron-phonon coupling, Phys. Rev. B **104**, 195116 (2021).

[44] H. Fehske, D. Ihle, J. Loos, U. Trapper, and H. Büttner, Polaron formation and hopping conductivity in the Holstein-Hubbard model, Z. Phys. B **94**, 91 (1994).

[45] D. Ihle, H. Fehske, J. Loos, and U. Trapper, Bi-/polaron formation and optical conductivity in the Holstein-Hubbard model, Physica C: Superconductivity **235-240**, 2363 (1994).

[46] G. Wellein, H. Röder, and H. Fehske, Polarons and bipolarons in strongly interacting electron-phonon systems, Phys. Rev. B **53**, 9666 (1996).

[47] J. Bonča, T. Katrašnik, and S. A. Trugman, Mobile Bipolaron, Phys. Rev. Lett. **84**, 3153 (2000).

[48] J. Bonča and S. A. Trugman, Bipolarons in the extended Holstein Hubbard model, Phys. Rev. B **64**, 094507 (2001).

[49] P. Werner and A. J. Millis, Efficient Dynamical Mean Field Simulation of the Holstein-Hubbard Model, Phys. Rev. Lett. **99**, 146404 (2007).

[50] H. Fehske, G. Hager, and E. Jeckelmann, Metallicity in the half-filled Holstein-Hubbard model, Europhys. Lett. **84**, 57001 (2008).

[51] D. Golež, J. Bonča, and L. Vidmar, Dissociation of a Hubbard-Holstein bipolaron driven away from equilibrium by a constant electric field, Phys. Rev. B **85**, 144304 (2012).

[52] A. Nocera, M. Soltanieh-ha, C. A. Perroni, V. Cataudella, and A. E. Feiguin, Interplay of charge, spin, and lattice degrees of freedom in the spectral properties of the one-dimensional Hubbard-Holstein model, Phys. Rev. B **90**, 195134 (2014).

[53] P. Werner and M. Eckstein, Field-induced polaron formation in the Holstein-Hubbard model, Europhys. Lett. **109**, 37002 (2015).

[54] F. Marsiglio, Impact of retardation in the Holstein-Hubbard model: a two-site calculation, arXiv:2205.10352.

[55] L. Vidmar, J. Bonča, S. Maekawa, and T. Tohyama, Bipolaron in the *t*-*J* Model Coupled to Longitudinal and Transverse Quantum Lattice Vibrations, Phys. Rev. Lett. **103**, 186401 (2009).

[56] L. Vidmar, J. Bonča, T. Tohyama, and S. Maekawa, Quantum Dynamics of a Driven Correlated System Coupled to Phonons, Phys. Rev. Lett. **107**, 246404 (2011).

[57] A. Szabó, S. A. Parameswaran, and A. Gopalakrishnan, High-temperature transport and polaron speciation in the anharmonic Holstein model, arXiv:2110.10170.

[58] J. H. Fetherolf, P. Shih, and T. C. Berkelbach, Conductivity of an electron coupled to anharmonic phonons, arXiv:2205.09811.

[59] N. C. Costa, T. Blommel, W.-T. Chiu, G. Batrouni, and R. T. Scalettar, Phonon Dispersion and the Competition between Pairing and Charge Order, Phys. Rev. Lett. **120**, 187003 (2018).

[60] C. Schönle, D. Jansen, F. Heidrich-Meisner, and L. Vidmar, Eigenstate thermalization hypothesis through the lens of autocorrelation functions, Phys. Rev. B **103**, 235137 (2021).

[61] D. J. J. Marchand and M. Berciu, Effect of dispersive optical phonons on the behavior of a Holstein polaron, Phys. Rev. B **88**, 060301(R) (2013).

[62] P. J. Robinson, I. S. Dunn, and D. R. Reichman, Cumulant methods for electron-phonon problems ii: The self-consistent cumulant expansion, Phys. Rev. B **105**, 224305 (2022).

[63] M. Capone, W. Stephan, and M. Grilli, Small-polaron formation and optical absorption in Su-Schrieffer-Heeger and Holstein models, Phys. Rev. B **56**, 4484 (1997).

[64] S. Fratini, F. de Pasquale, and S. Ciuchi, Optical absorption from a nondegenerate polaron gas, Phys. Rev. B **63**, 153101 (2001).

[65] G. Schubert, G. Wellein, A. Weisse, A. Alvermann, and H. Fehske, Optical absorption and activated transport in polaronic systems, Phys. Rev. B **72**, 104304 (2005).

[66] S. Fratini and S. Ciuchi, Optical properties of small polarons from dynamical mean-field theory, Phys. Rev. B **74**, 075101 (2006).

[67] G. Wellein and H. Fehske, Self-trapping problem of electrons or excitons in one dimension, Phys. Rev. B **58**, 6208 (1998).

[68] G. L. Goodvin, A. S. Mishchenko, and M. Berciu, Optical Conductivity of the Holstein Polaron, Phys. Rev. Lett. **107**, 076403 (2011).

[69] B. Bertini, F. Heidrich-Meisner, C. Karrasch, T. Prosen, R. Steinigeweg, and M. Žnidarič, Finite-temperature transport in one-dimensional quantum lattice models, Rev. Mod. Phys. **93**, 025003 (2021).

[70] S. R. White, Density Matrix Formulation for Quantum Renormalization Groups, Phys. Rev. Lett. **69**, 2863 (1992).

[71] U. Schollwöck, The density-matrix renormalization group, Rev. Mod. Phys. **77**, 259 (2005).

[72] U. Schollwöck, The density-matrix renormalization group in the age of matrix product states, Ann. Phys. (NY) **326**, 96 (2011).

[73] F. Verstraete, J. J. García-Ripoll, and J. I. Cirac, Matrix Product Density Operators: Simulation of Finite-Temperature and Dissipative Systems, Phys. Rev. Lett. **93**, 207204 (2004).

[74] A. J. Daley, C. Kollath, U. Schollwöck, and G. Vidal, Time-dependent density-matrix renormalization-group using adaptive effective Hilbert spaces, J. Stat. Mech. (2004) P04005.

[75] S. R. White and A. E. Feiguin, Real-Time Evolution Using the Density Matrix Renormalization Group, Phys. Rev. Lett. **93**, 076401 (2004).

[76] G. Vidal, Efficient Simulation of One-Dimensional Quantum Many-Body Systems, Phys. Rev. Lett. **93**, 040502 (2004).

[77] A. E. Feiguin and S. R. White, Finite-temperature density matrix renormalization using an enlarged Hilbert space, Phys. Rev. B **72**, 220401(R) (2005).

[78] T. Barthel, U. Schollwöck, and S. R. White, Spectral functions in one-dimensional quantum systems at finite temperature using the density matrix renormalization group, Phys. Rev. B **79**, 245101 (2009).

[79] E. M. Stoudenmire and S. R. White, Minimally entangled typical thermal state algorithms, New J. Phys. **12**, 055026 (2010).

[80] A. E. Feiguin and G. A. Fiete, Spectral properties of a spin-incoherent Luttinger liquid, Phys. Rev. B **81**, 075108 (2010).

[81] S. Paeckel, T. Köhler, A. Swoboda, S. R. Manmana, U. Schollwöck, and C. Hubig, Time-evolution methods for matrix-product states, Ann. Phys. (NY) **411**, 167998 (2019).

[82] C. Zhang, E. Jeckelmann, and S. R. White, Density Matrix Approach to Local Hilbert Space Reduction, Phys. Rev. Lett. **80**, 2661 (1998).

[83] E. Jeckelmann and S. R. White, Density-matrix renormalization-group study of the polaron problem in the Holstein model, Phys. Rev. B **57**, 6376 (1998).

[84] T. Köhler, J. Stolpp, and S. Paeckel, Efficient and flexible approach to simulate low-dimensional quantum lattice models with large local hilbert spaces, SciPost Phys. **10**, 058 (2021).

[85] S. Mardazad, Y. Xu, X. Yang, M. Grundner, U. Schollwöck, H. Ma, and S. Paeckel, Quantum dynamics simulation of intramolecular singlet fission in covalently linked tetracene dimer, J. Chem. Phys. **155**, 194101 (2021).

[86] J. Haegeman, J. I. Cirac, T. J. Osborne, I. Pižorn, H. Verschelde, and F. Verstraete, Time-Dependent Variational Principle for Quantum Lattices, Phys. Rev. Lett. **107**, 070601 (2011).

[87] J. Haegeman, C. Lubich, I. Oseledets, B. Vandereycken, and F. Verstraete, Unifying time evolution and optimization with matrix product states, Phys. Rev. B **94**, 165116 (2016).

[88] P. Secular, N. Gourianov, M. Lubasch, S. Dolgov, S. R. Clark, and D. Jaksch, Parallel time-dependent variational principle algorithm for matrix product states, Phys. Rev. B **101**, 235123 (2020).

[89] C. Lanczos, An iteration method for the solution of the eigenvalue problem of linear differential and integral operators, J. Res. Natl. Bur. Stand. **45**, 255 (1950).

[90] P. Prelovšek and J. Bonča, *Ground State and Finite Temperature Lanczos Methods, Ground State and Finite Temperature Lanczos Methods* (Springer, Berlin, Heidelberg, 2013), pp. 1–30.

[91] M. Born and R. Oppenheimer, Zur Quantentheorie der Molekeln, Annalen der Physik **389**, 457 (1927).

[92] M. Born and K. Huang, *Dynamical Theory of Crystal Lattices* (Clarendon Press, Oxford, 1954).

[93] M. Stone and P. Goldbart, *Mathematics for Physics: A Guided Tour for Graduate Students* (Cambridge University Press, New York, 2009).

[94] H. Reik and D. Heese, Frequency dependence of the electrical conductivity of small polarons for high and low temperatures, J. Phys. Chem. Solids **28**, 581 (1967).

[95] D. Emin, Optical properties of large and small polarons and bipolarons, Phys. Rev. B **48**, 13691 (1993).

[96] G. Mahan, *Many-Particle Physics* (Plenum, New York, 2000).

[97] G. C. Schatz and M. A. Ratner, *Quantum Mechanics in Chemistry* (Dover, Mineola, New York, 2002).

[98] A. Nitzan, *Chemical Dynamics in Condensed Phases* (Oxford University Press, New York, 2006).

[99] Y. A. Firsov and E. K. Kudinov, The polaron state of a crystal, Phys. Solid State **43**, 447 (2001).

[100] L. K. McKemmish, R. H. McKenzie, N. S. Hush, and J. R. Reimers, Electronvibration entanglement in the Born-Oppenheimer description of chemical reactions and spectroscopy, Phys. Chem. Chem. Phys. **17**, 24666 (2015).

[101] S. R. White, Minimally Entangled Typical Quantum States at Finite Temperature, Phys. Rev. Lett. **102**, 190601 (2009).

[102] M. Binder and T. Barthel, Minimally entangled typical thermal states versus matrix product purifications for the simulation of equilibrium states and time evolution, Phys. Rev. B **92**, 125119 (2015).

[103] T. Barthel, Matrix product purifications for canonical ensembles and quantum number distributions, Phys. Rev. B **94**, 115157 (2016).

[104] A. Nocera and G. Alvarez, Symmetry-conserving purification of quantum states within the density matrix renormalization group, Phys. Rev. B **93**, 045137 (2016).

[105] M. Urbanek and P. Soldán, Parallel implementation of the time-evolving block decimation algorithm for the bosehubbard model, Comput. Phys. Commun. **199**, 170 (2016).

[106] B. Kloss, Y. B. Lev, and D. Reichman, Time-dependent variational principle in matrix-product state manifolds: Pitfalls and potential, Phys. Rev. B **97**, 024307 (2018).

[107] B. Kloss, D. R. Reichman, and R. Tempelaar, Multiset Matrix Product State Calculations Reveal Mobile Franck-Condon Excitations Under Strong Holstein-Type Coupling, Phys. Rev. Lett. **123**, 126601 (2019).

[108] M. Yang and S. R. White, Time-dependent variational principle with ancillary Krylov subspace, Phys. Rev. B **102**, 094315 (2020).

[109] Y. Xu, Z. Xie, X. Xie, U. Schollwöck, and H. Ma, Stochastic adaptive single-site time-dependent variational principle, JACS Au **2**, 335 (2022).

[110] E. M. Stoudenmire and S. R. White, Real-space parallel density matrix renormalization group, Phys. Rev. B **87**, 155137 (2013).

[111] G. Vidal, Efficient Classical Simulation of Slightly Entangled Quantum Computations, Phys. Rev. Lett. **91**, 147902 (2003).

[112] C. Guo, A. Weichselbaum, J. von Delft, and M. Vojta, Critical and Strong-Coupling Phases in One- and Two-Bath Spin-Boson Models, Phys. Rev. Lett. **108**, 160401 (2012).

[113] C. Brockt, F. Dorfner, L. Vidmar, F. Heidrich-Meisner, and E. Jeckelmann, Matrix-product-state method with a dynamical local basis optimization for bosonic systems out of equilibrium, Phys. Rev. B **92**, 241106(R) (2015).

[114] A. E. Feiguin and S. R. White, Time-step targeting methods for real-time dynamics using the density matrix renormalization group, Phys. Rev. B **72**, 020404(R) (2005).

[115] C. Karrasch, J. H. Bardarson, and J. E. Moore, Finite-Temperature Dynamical Density Matrix Renormalization Group and the Drude Weight of Spin-1/2 Chains, Phys. Rev. Lett. **108**, 227206 (2012).

[116] T. Barthel, U. Schollwöck, and S. Sachdev, Scaling of the thermal spectral function for quantum critical bosons in one dimension, arXiv:1212.3570.

[117] T. Barthel, Precise evaluation of thermal response functions by optimized density matrix renormalization group schemes, New J. Phys. **15**, 073010 (2013).

[118] C. Karrasch, J. H. Bardarson, and J. E. Moore, Reducing the numerical effort of finite-temperature density matrix renormalization group calculations, New J. Phys. **15**, 083031 (2013).

[119] D. Kennes and C. Karrasch, Extending the range of real time density matrix renormalization group simulations, Comput. Phys. Commun. **200**, 37 (2016).

[120] J. Hauschild, E. Leviatan, J. H. Bardarson, E. Altman, M. P. Zaletel, and F. Pollmann, Finding purifications with minimal entanglement, Phys. Rev. B **98**, 235163 (2018).

[121] P. P. Vaidyanathan, *The Theory of Linear Prediction*, Synthesis Lectures on Engineering Series (Morgan & Claypool, San Rafael, 2008).

[122] S. R. White and I. Affleck, Spectral function for the $S = 1$ Heisenberg antiferromagetic chain, Phys. Rev. B **77**, 134437 (2008).

[123] Y. Tian and S. R. White, Matrix product state recursion methods for computing spectral functions of strongly correlated quantum systems, Phys. Rev. B **103**, 125142 (2021).

[124] M. Fishman, S. R. White, and E. M. Stoudenmire, The ITensor software library for tensor network calculations, arXiv:2007.14822 (2020).

[125] I. G. Lang and Yu. A. Firsov, Kinetic theory of semiconductors with low mobility, Zh. Eksp. Teor. Fiz. **43**, 1843 (1963) [Sov. Phys. JETP **16**, 1301 (1963)].

[126] P. Ehrenfest, Bemerkung über die angenäherte Gültigkeit der klassischen Mechanik innerhalb der Quantenmechanik, Z. Phys. **45**, 455 (1927).

[127] J. C. Tully, Molecular dynamics with electronic transitions, J. Chem. Phys. **93**, 1061 (1990).

[128] D. V. Shalashilin, Quantum mechanics with the basis set guided by Ehrenfest trajectories: Theory and application to spin-boson model, J. Chem. Phys. **130**, 244101 (2009).

[129] D. V. Shalashilin, Nonadiabatic dynamics with the help of multiconfigurational Ehrenfest method: Improved theory and fully quantum 24d simulation of pyrazine, J. Chem. Phys. **132**, 244111 (2010).

[130] G. Li, B. Movaghar, A. Nitzan, and M. A. Ratner, Polaron formation: Ehrenfest dynamics vs. exact results, J. Chem. Phys. **138**, 044112 (2013).

[131] P. Mitrić, V. Janković, N. Vukmirović, and D. Tanasković, Spectral Functions of the Holstein Polaron: Exact and Approximate Solutions, Phys. Rev. Lett. **129**, 096401 (2022).

[132] P. J. Robinson, I. S. Dunn, and D. R. Reichman, Cumulant methods for electron-phonon problems i: Perturbative expansions, Phys. Rev. B **105**, 224304 (2022).

[133] J. L. Alonso, C. Bouthelier-Madre, A. Castro, J. Clemente-Gallardo, and J. A. Jover-Galtier, About the computation of finite temperature ensemble averages of hybrid quantum-classical systems with molecular dynamics, New J. Phys. **23**, 063011 (2021).

[134] V. Janković and N. Vukmirović, Spectral and thermo-dynamic properties of the Holstein polaron: Hierarchical equations of motion approach, Phys. Rev. B **105**, 054311 (2022).

[135] M. ten Brink, S. Gräber, M. Hopjan, D. Jansen, J. Stolpp, F. Heidrich-Meisner, and P. E. Blöchl, Real-time non-adiabatic dynamics in the one-dimensional Holstein model: Trajectory-based vs exact methods, J. Chem. Phys. **156**, 234109 (2022).

[136] T. Hotta and E. Dagotto, *Theory of Manganites* (Springer, Dordrecht, 2004).

[137] D. Jansen, J. Bonča, and F. Heidrich-Meisner, https://arxiv.org/src/2206.00985v2/anc.

[138] F.-Z. Chen, C. Cheng, and H.-G. Luo, Real-space parallel density matrix renormalization group with adaptive boundaries, Chin. Phys. B **30**, 080202 (2021).

[139] P. E. Kornilovitch, Photoemission spectroscopy and sum rules in dilute electron-phonon systems, Europhys. Lett. **59**, 735 (2002).

[140] G. L. Goodvin, M. Berciu, and G. A. Sawatzky, Green's function of the Holstein polaron, Phys. Rev. B **74**, 245104 (2006).

[141] A. Tokmakoff, Lecture notes on time-dependent quantum mechanics and spectroscopy (unpublished).

Correction: The omission of a data availability statement has been rectified.